

The size–density relation of extragalactic H II regions

L. K. Hunt¹ and H. Hirashita²

¹ INAF - Osservatorio Astrofisico di Arcetri, Largo E. Fermi, 5, 50125 Firenze, Italy
e-mail: hunt@arcetri.astro.it

² Institute of Astronomy and Astrophysics, Academia Sinica, P.O. Box 23-141, Taipei 10617, Taiwan
e-mail: hirashita@asiaa.sinica.edu.tw

2 September 2009

ABSTRACT

Aims. We investigate the size–density relation in extragalactic H II regions, with the aim of understanding the role of dust and different physical conditions in the ionized medium.

Methods. First, we compiled several observational data sets for Galactic and extragalactic H II regions and confirm that extragalactic H II regions follow the same size (D)–density (n) relation as Galactic ones ($n \propto D^{-1}$), rather than a relation with constant luminosity ($n \propto D^{-1.5}$). Motivated by the inability of static models to explain this, we then modelled the evolution of the size–density relation of H II regions by considering their star formation history, the effects of dust, and pressure-driven expansion. The results are compared with our sample data whose size and density span roughly six orders of magnitude.

Results. The extragalactic samples cannot be understood as an evolutionary sequence with a single initial condition. Thus, the size–density relation does not result from an evolutionary sequence of H II regions but rather reflects a sequence with different initial gas densities (“density hierarchy”). We also find that the size of many H II regions is limited by dust absorption of ionizing photons, rather than consumption by ionizing neutral hydrogen. Dust extinction of ionizing photons is particularly severe over the entire lifetime of compact H II regions with typical gas densities of $\gtrsim 10^3 \text{ cm}^{-3}$. Hence, as long as the number of ionizing photons is used to trace massive star formation, much star-formation activity could be missed. Such compact dense environments, the ones most profoundly obscured by dust, have properties similar to “maximum–intensity starbursts”. This implies that submillimeter and infrared wavelengths may be necessary to accurately assess star formation in these extreme conditions both locally and at high redshift.

Key words. dust, extinction – galaxies: dwarf – galaxies: evolution – galaxies: ISM – galaxies: star clusters – H II regions

1. Introduction

Massive stars, young star clusters, and their associated H II regions are vital probes of recent star formation in nearby galaxies and the distant universe. While Galactic H II regions such as the Orion Nebula and RCW 49 are well studied because of their proximity, most Galactic work is still plagued by distance uncertainties (e.g., Anderson & Bania 2009), although the situation is improving rapidly (see, e.g., Hachisuka et al. 2006, Foster & MacWilliams 2006, Russeil et al. 2007). H II regions in galaxies in the Local Group can be studied in almost as much detail as those in the Galaxy, and the distance estimation is much less uncertain. However, even in Local Group galaxies, Super Star Clusters (SSCs), the most extreme examples of massive star formation, are absent. SSCs, with $\sim 10^5$ – $10^6 M_\odot$ and Lyman continuum photon rates $\dot{N}_{\text{ion}} \sim 10^{52}$ – 10^{53} s^{-1} enclosed in regions of $\lesssim 10 \text{ pc}$ in radius, are generally not seen in quiescent environments such as the Milky Way, M 31, and M 33. Even R136 in 30 Doradus, the most massive Local Group star cluster ($10^{4.5} M_\odot$ and $10^{51.4} \text{ s}^{-1}$; Massey & Hunter 1998), falls short of the typical properties of SSCs. Hence, to study the wide range of manifestations of massive star formation, it is necessary to examine star clusters and H II regions in galaxies beyond the Local Group. Of necessity, the price to be paid is detail; the advantage to be gained is the wide variety of Star-Forming (SF) complexes that can be studied.

The total mass of a cluster of massive stars can be observationally quantified by estimating the number of ionizing photons. A simple Strömgren-sphere argument (Eq. 2) would suggest that

$\dot{N}_{\text{ion}} \propto D^3 n_e^2$, where \dot{N}_{ion} is the number of ionizing photons emitted per unit time, D is the diameter of the H II region, and n_e is the electron number density in the H II region. Thus, in principle, by examining n_e and D of H II regions, we can estimate the ionizing photon luminosity. However, observationally, the situation is not straightforward. The diameter (D) and the electron density (n_e) of Galactic H II regions are known to be negatively correlated with a roughly unit slope: $n_e \propto D^{-1}$ (Garay & Lizano 1999; Kim & Koo 2001; Martín-Hernández et al. 2003; Dopita et al. 2006). This would not be expected from a simple Strömgren-sphere argument with \dot{N}_{ion} constant: $n_e \propto D^{-1.5}$. Various possible explanations for the observed shallower slope are presented in Martín-Hernández et al. (2003), including optical depth effects, clumpiness, dust extinction, and stellar content. Dust mixed in with the ionized gas has also been proposed as an explanation by Arthur et al. (2004, hereafter A04) who argue that significant absorption of ionizing photons by dust grains in the densest H II regions flattens the size–density relation.

Previous work on extragalactic H II regions suggests that they follow the same size–density correlation as Galactic ones. Kennicutt (1984) found that H II regions in spiral disks follow a $n_e \propto D^{-1}$ relation, but extend the Galactic trend to lower densities and larger sizes. More recently, Gilbert & Graham (2007) examined the SSCs in the Antennae galaxies, a prototypical starburst merger, and found that these also follow the $n_e \propto D^{-1}$ relation. However, the SSCs in the Antennae have densities (~ 40 – 400 cm^{-3}) and sizes (25–100 pc) that place them on a different location in the n_e – D plane than the Kennicutt sample.

In fact, Gilbert & Graham (2007) conclude that the SSCs in the Antennae constitute a new class of massive H II regions that is distinct from the Galactic and typical extragalactic population.

In this paper, we examine the size–density relation in extragalactic H II regions, and explore several mechanisms which have been proposed to explain it, including clumpiness, dust extinction, and stellar content. In particular, we focus on the H II regions in Blue Compact Dwarf galaxies (BCDs); following Gilbert & Graham (2007), we shall refer to such regions as Emission-Line Clusters (ELCs). In fact, most of the current star formation in many BCDs occurs in such ELCs, rather than in the underlying diffuse component. Previously we studied a more limited sample, and found that the H II regions in BCDs also follow the same size–density relation namely, $n_e \propto D^{-1}$ (Hunt et al. 2003). Here we triple the sample size used in our previous work, and compare the BCD ELCs with other types of extragalactic H II regions, such as those in spiral disks and known SSCs.

Focusing on BCDs enables us to study another aspect of the formation of star clusters. Because they are generally metal poor, with oxygen abundances [$12 + \log(\text{O}/\text{H})$] ranging from 7.2 to 8.5 (Izotov, Thuan, & Stasińska 2007), BCDs provide a link between high-redshift metal-free primeval galaxies and the metal-enriched SF galaxies in the local universe. Because metallicity is not expected to be the only driver of star-formation and cluster properties, we can compare different metallicities together with other parameters, and better disentangle the effects of metal abundance.

In fact, the process of ionization itself in metal-poor objects is also important in the cosmological context. Because they are relatively chemically unevolved, H II regions in BCDs could enable us to infer some characteristics of the ionization processes at high z . Since the typical virial temperature of the first-generation objects in the Universe is $\lesssim 10^4$ K (e.g., Tegmark et al. 1997; Yoshida et al. 2003), the photoionization which raises the gas temperature to $\sim 10^4$ K prohibits the gas from collapsing to form stars (Omukai & Nishi 1999). The gas density structure is modified by the pressure-driven expansion of H II regions (Kitayama et al. 2004). Such effects on the gas structure are of fundamental importance for considering the subsequent star formation and the reionization of the Universe.

The relation $n_e \propto D^{-1}$ for Galactic and extragalactic H II regions can be interpreted as a *constant ionized-gas column density*. However, the physical mechanism that produces the constant column density is not clear, nor is it clear why ELCs in external galaxies and Galactic H II regions should follow a similar relation with column density. It is also not understood whether or not there are different classes of H II regions which would occupy distinct zones of parameter space in the size–density plane, and if there are, how they might be related.

The aim of this paper is to understand the size–density relation of extragalactic H II regions, and place it in the context of star-cluster and ELC formation. The paper is organized as follows. First, in Sect. 2, we describe the observational samples of extragalactic H II regions, together with the compilation of Galactic H II regions for comparison. In Sect. 3, we examine gross trends in the data, which we will later interpret in the light of our evolutionary models. We predict the size–density relation for *static* dusty H II regions by assuming a constant luminosity of the central sources in Sect. 4. Then, in Sect. 5, we extend the model to include pressure-driven expansion and star formation history. Some basic results of this evolutionary model are given in Sect. 6, and compared with the extragalactic observational data. In Sect. 7 we discuss the models and their impli-

cations in various contexts. Finally we give our conclusions in Sect. 8. We adopt a Hubble constant of $H_0 = 73 \text{ km s}^{-1} \text{ Mpc}^{-1}$.

2. The data

We have assembled several samples of H II regions from the literature, including two extragalactic and two Galactic radio data sets, and one extragalactic optical sample. Another extragalactic optical sample is presented here for the first time, with sizes measured from *HST* images and electron densities derived from emission measures calculated with published long-slit optical spectra.

2.1. Extragalactic radio data sets

One extragalactic radio data set comprises those galaxies with known “ultra-dense H II regions” or “radio super nebulae” (see Koblunicky & Johnson 1999, Beck et al. 2002). Many of these are found in low-luminosity low-metallicity BCDs, but some reside in metal-rich starbursts such as NGC 253 and M 82 and normal spiral disks, including NGC 4214 and NGC 6946. The common feature of these multifrequency radio continuum observations is a rising spectrum at low frequencies, and a relatively flat spectrum at higher ones. This implies that the predominant emission mechanism is thermal bremsstrahlung from ionized gas, and that the electron density and size are such that there is a turnover in the radio spectrum at some frequency ν_t . This “turnover frequency” ν_t corresponds to an optical depth τ_ν of unity, and defines the frequency where the spectrum changes from optically thick to optically thin. ν_t depends on the Emission Measure ($\text{EM} = \int n_e^2 d\ell$) and the electron temperature T_e . The spectra of “classical” H II regions such as Orion turn over at very low frequencies, ~ 0.3 GHz, while the compact dense regions in these galaxies have $\nu_t \gtrsim 5$ GHz. All radio observations described below measure the high-frequency optically thin part of the radio spectrum ($F_\nu \propto \nu^{-0.1}$), as well as the transition region ($\nu \lesssim \tau_\nu$) toward lower frequencies where the spectrum becomes optically thick.

In some cases, with high-resolution observations (II Zw 40: Beck et al. 2002; NGC 5253: Turner et al. 2000), the radio emission is resolved at 15 GHz. Thus, the authors were able to estimate the size D of the emitting region by fitting a Gaussian, and from the observed flux, determine the EM, and infer the rms electron density $\langle n_e \rangle$. In other cases (NGC 4214, NGC 1741, Mrk 8, Mrk 33, VII Zw 19, Pox 4, Tol 35, Mrk 1236: Beck et al. 2000; NGC 6946, NGC 253, M 33: Johnson et al. 2001; SBS 0335-052: Hunt et al. 2004, Johnson et al. 2009), the spatial resolution is insufficient to resolve the regions. Then the radio spectrum can be fit by models of homogeneous, isothermal, dust-free, ionization bounded regions of ionized gas, to obtain the turnover frequency ν_t , the EM, $\langle n_e \rangle$, and infer the size D of the region (e.g., Deeg et al. 1993; Johnson et al. 2001; Hunt et al. 2004). Alternatively, the optically thick and optically thin regions of the radio spectrum can be separated to constrain ν_t , and thus infer the emission measure EM, size D , and rms electron density $\langle n_e \rangle$ (e.g., Gordon 1988; Beck et al. 2000). When the size is not directly measured, that is to say when the sources are unresolved, the authors estimate sizes and densities from fits of multi-frequency radio continuum spectra; these are consequently not independent parameters, but rather negatively correlated. Nevertheless, the logarithmic slope between density and size expected from this degeneracy would be -1.5 which is significantly steeper than that observed (see below). The sizes D

and densities $\langle n_e \rangle$ for NGC 5253 and He 2–10 have been modeled also from radio recombination line observations, and are consistent with those inferred from continuum fitting (Mohan et al. 2001).

There is one galaxy in our data set, IZw 18, in which multi-frequency observations show no sign of a rising spectrum (Hunt et al. 2005). Here also the data have been fit to a model of an homogeneous, isothermal, dust-free ionization bounded region of ionized gas, as described above.

We will refer to this sample of (except for IZw 18) rising-spectrum sources as the “radio sample” (16 galaxies); its mean oxygen abundance is $12+\log(\text{O}/\text{H}) = 8.24 \pm 0.5$, or $\sim 0.22 Z_\odot$ ¹. When there are multiple observations for a single object, we usually list these data as different data points. However, M 33, NGC 253, and NGC 6946 contain several candidates for ultra-compact H II regions, but we show each galaxy as a single average according to the figures in Johnson et al. (2001). The data for the radio sample are reported in Table 1; all sizes have been corrected to the distance scale used here.

The other extragalactic radio sample comprises H II regions in the Small and Large Magellanic Clouds (SMC and LMC, respectively) (Martín-Hernández et al. 2005), and in the super-giant H II region NGC 604 in M 33 (Churchwell & Goss 1999). As with the previous data set, these are also radio continuum observations, but at a single frequency, 5 GHz (SMC/LMC) or 8.4 GHz (NGC 604/M 33). We adopt the results given in the original papers for sizes D and densities $\langle n_e \rangle$. The regions in these Local Group galaxies are resolved, and D is measured from high-resolution interferometric maps by fitting two-dimensional Gaussians, including beam deconvolution. The densities are inferred from the observed flux densities by assuming that all radio emission is optically thin bremsstrahlung, arising in a dust-free, ionization bounded, homogeneous region with size D (Mezger & Henderson 1967). This sample will be called the “Local-Group sample”; with M 33, the LMC, and the SMC, its mean oxygen abundance is $12+\log(\text{O}/\text{H}) = 8.41 \pm 0.3$, corresponding to $0.33 Z_\odot$.

2.2. Galactic radio samples

We have also included two size–density data sets of Galactic H II regions as comparison samples. The first Galactic sample is taken from the compilation by Garay & Lizano (1999), and consists of compact H II regions observed with high angular resolution in either the H66 α or H76 α lines, as well as in the radio continuum. The second sample is a set of (ultra) compact Galactic H II regions, observed in the 21 cm radio continuum by Kim & Koo (2001). For both samples, we have adopted the authors’ H II region parameters; the electron densities were derived assuming optically thin, dust-free, homogeneous, ionization-bounded nebulae (e.g., Mezger & Henderson 1967), and the sizes were directly measured from interferometric radio images by fitting Gaussians, deconvolved with the beam size. As in the Local-Group sample, such measurements obviate the potential density–size degeneracy with logarithmic slope -1.5 that could arise were the sizes not measured independently.

2.3. HST extragalactic optical sample

The main optical sample includes those star-forming dwarf galaxies with optical spectra and usable high-resolution *Hubble*

Space Telescope (HST) archival data, obtained either with the Advanced Camera for Surveys (ACS), the Wide Field Planetary Camera 2 (WFPC2), or in the near-infrared with the NICMOS array. Most of the images were retrieved from the Hubble Legacy Archive². We obtained images for 26 galaxies, but use only 23 of them; 3 had only F160W images, and when images at other wavelengths were available for comparison, the F160W images gave consistently larger sizes than the other wavelengths. Virtually all of the galaxies are BCDs.

The high resolution of *HST* is crucial in order to resolve the ELCs in the sample objects. Most of the galaxies are dominated by a single bright SF complex; because we want to compare with ground-based long-slit optical spectra, this is the region we focus on, rather than examining the more diffuse emission. There were generally no H α images available, so we were forced to use the continuum to determine the size of the SF region. Since we wanted to match the size measurement as much as possible with the spectroscopic slit, we adopted a one-dimensional method rather than two-dimensional models as in the radio. For each galaxy, we measured the linear extent by fitting the surface brightness profiles in two orthogonal cuts with Lorentzian and Gaussian profiles. Although Lorentzians fit the extended wings of the profiles better than Gaussians, they give widths that are $\sim 8\%$ smaller. Hence, we adopted the Gaussian fits to be compatible with the analogous fits for the radio source sizes. The *HST* profiles are extracted in 1-arcsec wide rectangular apertures, which match the spectroscopic slit (i.e., with roughly the same spatial resolution as the H β measurements adopted below). The diameter of the region is defined as the geometrical mean of the full widths at half maximum (FWHMs) of these two orthogonal (Gaussian) profiles. If data are available in more than one band, we adopt the longest-wavelength data with the highest spatial resolution, although there is no significant trend of sizes with filter band (except for F160W as noted above). Despite the high spatial resolution of the *HST*, we were unable to resolve the brightest complex in a few distant galaxies with particularly compact SF regions. In those cases, we will be overestimating the region size, and consequently underestimating the root-mean-square electron density; these will be discarded in the analysis.

In general, it should be emphasized that the size measurement is a delicate and difficult procedure. Many of the objects have blended regions which *HST* did not resolve, but which would fall within a ground-based spectroscopic slit. Moreover, because most of the spectroscopic observations did not give the position angle of the slit, we had to use subjective judgment to determine the angles for our virtual cut apertures. It is also true that ionized gas in an ELC tends to be more extended than the underlying nebular continuum and stellar emission, so we are probably underestimating the size with our method and account for this empirically (see below). All these considerations make the diameter determinations only good to a factor of 2 or so, but the consistency with the other samples lends confidence to the procedure.

The root-mean-square (rms) number densities $\langle n_e \rangle$ are calculated from long-slit observations of the optical H β recombination line. Following Kennicutt (1984), we convert the H β surface brightness over the spectroscopic slit area to volume emission measure. Hydrogen emissivities are calculated with ionized-gas

¹ In this and future relative solar abundances, we will adopt the solar calibration of Anders & Grevesse (1989).

² The Hubble Legacy Archive is a collaboration between the Space Telescope Science Institute (STScI/NASA), the Space Telescope European Coordinating Facility (ST-ECF/ESA) and the Canadian Astronomy Data Centre (CADM/NRC/CSA).

temperatures inferred from optical emission lines, as given by published tables (see Table 2). Extinction is corrected for with published values of $c(H\beta)$, and ionized helium with a multiplicative factor of 1.08. The continuum size of an ELC is generally 1.5 to 2 times smaller than the ionized gas extent (Tenorio-Tagle et al. 2006, Silich et al. 2007), so to convert the volume emission measure to rms density $\langle n_e \rangle$, we have adopted a region size 1.5 times as large as actually measured in the continuum. To account for the larger extension of the ionized gas relative to the continuum, we also used this enlarged size as the “true size” of the H II regions measured from the images. Because of the considerable uncertainties in this entire procedure, the densities $\langle n_e \rangle$ are probably only good to roughly a factor of 2, being slightly less uncertain than the diameters because of the square-root dependence on EM. Nevertheless, this is similar to the uncertainty in the rising-spectrum radio sample, and to the comparison optical sample described in Sect. 2.4. The sample, which we call the “*HST* sample”, is given in Table 2, together with the references for the spectroscopic data. The mean oxygen abundance of the *HST* sample (23 galaxies) is $12+\log(O/H) = 7.89 \pm 0.35$, $\sim 0.09 Z_\odot$.

The rms densities $\langle n_e \rangle$ for the *HST* sample are plotted against the densities determined from the [S II] optical emission lines $n_e([S II])$ in Fig. 1. Similarly to previous work (Kennicutt 1984; Rozas et al. 1998), the densities inferred from the [S II] line ratio $n_e([S II])$ are much higher than the rms values $\langle n_e \rangle$ inferred from the emission measure. This is because the densities measured *in situ* from line ratios tend to be weighted toward high-density high surface-brightness knots which occupy a small fraction of the total volume (e.g., Zaritsky et al. 1994; Kennicutt 1984). The difference between the two kinds of measurements suggests that the ionized gas is clumpy, with dense knots in a more diffuse envelope (Kennicutt 1984; Zaritsky et al. 1994; Rozas et al. 1998). In a homogeneous medium with optically thin dense clumps, the volume filling factor (FF) relates the rms density and the sulfur-derived one: $\sqrt{\delta} = \langle n_e \rangle / n_e([S II])$, where δ signifies the filling factor. Constant volume FFs are shown in Fig. 1; the data appear equally distributed from FFs of roughly unity to 10^{-3} . The filling factors are slightly lower, although comparable to those in H II regions in quiescent spiral disks (Kennicutt 1984). In general, the *HST* sample follows the same trends in size and density as the other samples, and appears to be consistent with them. The six galaxies with FWHM < 4.5 pixels in the *HST* images are marked with an arrow in Fig. 1. We are underestimating the rms densities and overestimating the sizes for these unresolved sources, and they are not considered in subsequent analysis.

2.4. Comparison extragalactic optical sample

The second optical sample is taken from the cornerstone study of giant H II regions in nearby spiral galaxies (Kennicutt 1984). With ground-based photographic $H\alpha$ emission-line images, Kennicutt used a spherically symmetric shell model and solved the Abelian integral for the emission-measure profile. Most of the profiles are monotonically decreasing with radius. One of the ELCs measured by Kennicutt, M82-A, has also been recently measured by another group; the old values of (450 pc, 16 cm^{-3} ; Kennicutt 1984) are now found to be (4.5 pc, 1800 cm^{-3} ; Silich et al. 2007). Another object is in common with our sample, Mrk 71 (NGC 2366A=NGC 2363): the old values are (560 pc, 4 cm^{-3}), in contrast with our new estimate of 14.4 pc (this includes the doubling described above), 149 cm^{-3} . The *HST* image of Mrk 71 gives a diameter of

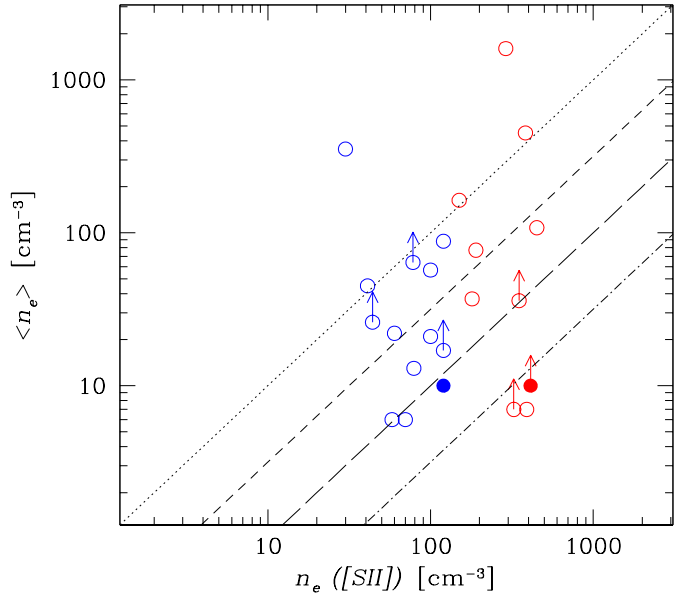


Fig. 1. RMS densities $\langle n_e \rangle$ vs. published densities inferred from the [S II] lines at $\lambda\lambda 6717, 6731 \text{ \AA}$ for the *HST* sample. The diagonal lines correspond to constant volume filling factors of 1 (dotted), 0.1 (short dashed), 0.01 (long dashed), and 0.001 (dot-dashed). The filled circles correspond to IZw 18 ($n_e([S II]) = 120 \text{ cm}^{-3}$), and SBS 0335–052 ($n_e([S II]) = 412 \text{ cm}^{-3}$), respectively. The red circles correspond to $n_e([S II]) > 125 \text{ cm}^{-3}$, and the blue ones to $n_e([S II]) < 125 \text{ cm}^{-3}$. The arrows show those galaxies with unresolved sizes, and thus underestimated $\langle n_e \rangle$; these objects are not considered further.

7.5 pixels ($\sim 0''.75$), and clearly resolves the SF complex; this corresponds to only the brightest portion of the region measured by Kennicutt, apparently not resolved by the ground-based photographic images. It is clear that the larger the region over which the density is averaged, the smaller the rms density. It is noteworthy that all these measurements, old and new, follow the same relation between size and density, as discussed below.

3. Overall empirical trends

The size–density relation of the samples is shown in Fig. 2. All Galactic and extragalactic samples can be fit by $n_e \propto D^{-1}$ to within the uncertainties in the slope. This behavior was already noted for the Galactic samples by Garay & Lizano (1999) and by Kim & Koo (2001). Fig. 2 shows the best-fit regressions for the Kim & Koo sample, the Garay & Lizano sample, and the extragalactic radio sample, but with the slopes slightly tweaked to be exactly unity; the intercepts for the three regressions ($\log n_e [\text{cm}^{-3}]$ at diameter = 1 pc) are 2.8, 3.5, and 4.4, from bottom to top, respectively. At face value, these offsets would imply that the mean column densities in the ionized gas increase by almost two orders of magnitude, going from compact to ultra-compact Galactic H II regions, to ultra-dense extragalactic H II regions (the radio sample). The size–density relation in all H II regions, Galactic and extragalactic, is clearly flatter than that produced in a homogeneous Strömgen sphere with a constant luminosity of ionizing photons ($n_e \propto D^{-1.5}$; Sect. 4).

The trends of the different samples also suggest that metallicity is not the key factor in H II region properties. While at approximately the same metal abundance, some of the regions in

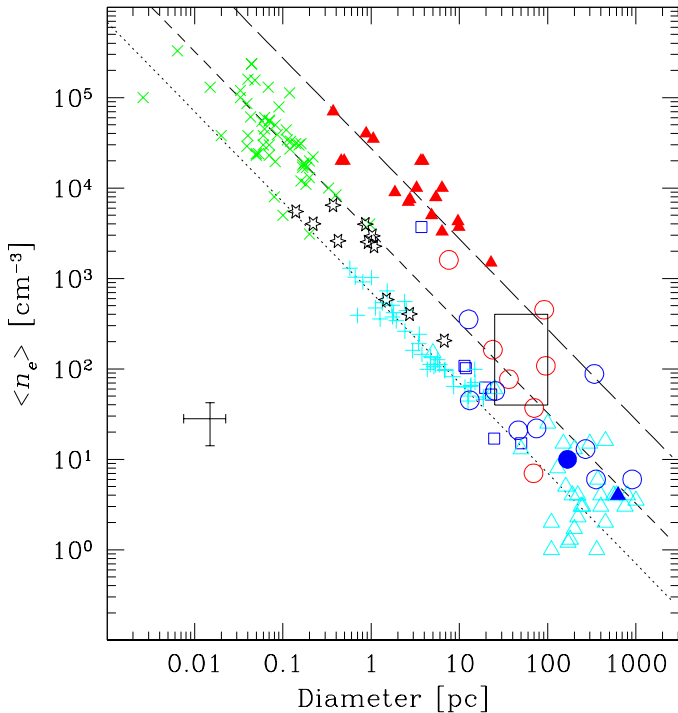


Fig. 2. Densities n_e vs. size (diameter) of the six H II-region samples. The extragalactic radio sample (except for M 33 and I Zw 18) is shown by filled (red) triangles; (the radio data for) I Zw 18 by a filled blue triangle; M 33 by open (blue) squares; the Garay & Lizano (1999) sample by (green) \times ; the LMC/SMC by (black) open stars; the Kim & Koo (2001) sample by (cyan) $+$; the Kennicutt (1984) sample by open (cyan) triangles; the *HST* sample by open (red and blue) circles, except for I Zw 18 which is shown by a filled (blue) circle. SBS 0035–052 has been excluded from our *HST* sample because it is unresolved. The large rectangle shows the range of sizes and densities for the SSCs in the Antennae galaxies (Gilbert & Graham 2007). Root-mean-square densities $\langle n_e \rangle$ (cm^{-3}) are shown for the *HST* sample, with sizes and $\langle n_e \rangle$ calculated as described in the text. The red circles have [S II]-inferred densities of $\geq 125 \text{ cm}^{-3}$, and blue circles $\leq 125 \text{ cm}^{-3}$. The regression lines are unit slopes (the same as the best fit, to within the errors) with intercepts of 2.8, 3.5, and 4.4. A factor-of-two error bar is shown in the lower left corner.

the Local-Group sample lie closer to the dense compact Galactic sample, while others are coincident with the less dense Galactic sample. Both Galactic samples are of roughly solar metallicity, but their locations differ from one another in the size–density plane. Lastly, the mean metallicity of the ultra-dense radio sample is only slightly lower than solar, but they lie far away from the locus of the (roughly solar abundance) H II regions in spiral disks.

Except for the radio sample, most of the extragalactic H II regions follow the same size–density trend as the Galactic ones. In particular, a large part of the *HST* sample BCDs are located at the extension of the size–density relation of the Galactic and Local-Group samples, coincident with the H II regions found in spiral disks. The correlation of size and density in the *HST* sample alone is highly significant; with a parametric correlation coefficient $r = -0.66$, the (one-tailed) significance level is $\geq 99.8\%$.

3.1. Emission measure and density systematics

All the densities in the size–density relation presented here are derived from the EM of either free-free radio emission or hydrogen recombination lines in the optical. Because $\text{EM} \propto D$, we might expect the size–density relation to result from constant EM over a sample, combined with a constant luminosity as in the Strömgren argument. The first would result in $\langle n_e \rangle \propto D^{-1/2}$, and the second would give $\langle n_e \rangle \propto D^{-3/2}$; combining the effects would tend to flatten the slope from the Strömgren relation.

However, we can exclude this as the reason for the unit slope in the data presented above, and in previous work by other groups. The EMs in the Galactic radio samples vary by more than four orders of magnitude; the same is true for the optically-inferred EMs in the *HST* sample. This would refute the hypothesis of a constant EM. Moreover, we have verified that the densities inferred from the S II lines for the *HST* sample are also correlated with the size D . These optical measurements are independent of the EM inferred from the hydrogen lines, and thus should provide a robust check of systematics. Because the sulfur lines do not probe densities significantly below $\sim 100 \text{ cm}^{-3}$, we exclude S II densities with values $< 50 \text{ cm}^{-3}$, and find a correlation coefficient of $r = -0.46$. This is a weaker correlation than the one with rms densities $\langle n_e \rangle$, but still significant at the 96% level. Since the S II densities are independent of the emission measure, we conclude that the size–density relation is not spuriously induced by the method used to infer rms electron densities.

3.2. Scale-free star formation

The power-law size–density relation of H II regions suggests that massive star formation is self-similar, that is, there is no characteristic scale of star formation. This scale-free nature was already noted by Larson (1981) who found an approximately unit slope between the rms H_2 volume density and the size of molecular clouds: $\langle n(\text{H}_2) \rangle (\text{cm}^{-3}) = 3400 L(\text{pc})^{-1.1}$. Kim & Koo (2001) found a similar relation relating Galactic H II region density and size, and argued that it reflects a variation of the ambient density, rather than an evolutionary effect. Indeed, the similarity of the size–density trend for molecular clouds and H II regions suggests that the star-formation processes retain an *imprint* from the molecular environment in which they take place.

This scale-free nature of H II regions is also supported by the data presented here. Three BCDs, He 2–10, SBS 0335–052, and II Zw 40, host both ultra-dense radio nebulae (see Table 1), and optically-visible H II regions (see Table 2). All these data follow the same size–density relation, but with different offsets. This implies that when the same regions are probed with longer dust-penetrating wavelengths and higher spatial resolution, they turn out to be denser and smaller, but with the same size–density relation as for the larger complexes. H II regions and hierarchical star formation will be discussed further in Sect. 7.4.

4. Static models

First, we interpret the size–density relation of the H II regions compiled in Sect. 2 by using simple theoretical arguments. In particular, we relate the size and density of H II regions for an ionizing point source embedded in a uniform and static medium with constant \dot{N}_{ion} . In such a situation, the radius of the ionized region can be estimated by the Strömgren radius (Spitzer 1978). We also include the effect of dust extinction, which is thought to be important in determining the size of H II regions (e.g., Inoue et

al. 2001, A04). The models described here are static models, and assume a number of ionizing photons \dot{N}_{ion} constant over time.

4.1. Size–density relation of dusty static H II regions

Here, we estimate the radius up to which the central source can ionize in a dusty uniform medium; this radius is called the ionization radius, r_i . Before estimating r_i , we define the Strömgen radius, r_S , as

$$\frac{4\pi}{3} r_S^3 n_e n_H \alpha^{(2)} = \dot{N}_{\text{ion}}, \quad (1)$$

where $\alpha^{(2)} = 2.6 \times 10^{-13} \text{ cm}^3 \text{ s}^{-1}$ is the recombination coefficient³ excluding captures to the ground ($n = 1$) level (Case B), n_H is the number density of hydrogen nuclei, and n_e is the electron density estimated by $n_e = 1.08 n_H$, where the factor 1.08 indicates the correction for helium ionization. Numerically, the Strömgen radius is estimated as

$$r_S = 1.4 \left(\frac{n_H}{10^2 \text{ cm}^{-3}} \right)^{-2/3} \left(\frac{\dot{N}_{\text{ion}}}{10^{48} \text{ s}^{-1}} \right)^{1/3} \text{ pc}. \quad (2)$$

In the absence of dust, the ionizing radius r_i would be equal to r_S . However, since a certain fraction of ionizing photons are absorbed by dust grains, the ionization radius r_i is reduced by a factor of $y_i (< 1)$, which is determined by solving (Petrosian et al. 1972; Spitzer 1978; A04)

$$3 \int_0^{y_i} y^2 e^{y \tau_{\text{Sd}}} dy = 1, \quad (3)$$

where τ_{Sd} is the dust optical depth for the ionizing photons over a path length equal to the Strömgen radius. This integral can be expanded:

$$1 = \frac{3y_i^2}{\tau_{\text{Sd}}} e^{\tau_{\text{Sd}} y_i} - \frac{6y_i}{\tau_{\text{Sd}}^2} e^{\tau_{\text{Sd}} y_i} + \frac{6}{\tau_{\text{Sd}}^3} (e^{\tau_{\text{Sd}} y_i} - 1) \quad (4)$$

In the optically thin limit ($\tau_{\text{Sd}} \ll 1$), Eq. (4) becomes $y_i \approx 1 - \tau_{\text{Sd}}/4$. Thus, we confirm that $y_i \rightarrow 1$ (i.e., $r_i \rightarrow r_S$) as $\tau_{\text{Sd}} \rightarrow 0$.

Once we obtain y_i for a value of τ_{Sd} (given in Sect. 4.2), the ionization radius can be estimated as

$$r_i = y_i r_S. \quad (5)$$

We also define the optical depth over the ionization radius as

$$\tau_{\text{di}} = y_i \tau_{\text{Sd}}. \quad (6)$$

4.2. Dust optical depth τ_{Sd}

In the above, we have left τ_{Sd} undetermined. Hirashita et al. (2001, see Appendix A for an alternative derivation) estimate it under a uniform dust-to-gas mass ratio \mathcal{D} as

$$\tau_{\text{Sd}} = 0.87 \left(\frac{\mathcal{D}}{6 \cdot 10^{-3}} \right) \left(\frac{n_H}{10^2 \text{ cm}^{-3}} \right)^{1/3} \left(\frac{\dot{N}_{\text{ion}}}{10^{48} \text{ s}^{-1}} \right)^{1/3}. \quad (7)$$

The dust-to-gas ratio of the solar neighborhood is assumed to be $\mathcal{D}_{\odot} = 6 \cdot 10^{-3}$ (Spitzer 1978). We adopt various constant values

³ This value is for a gas temperature of $T = 10000 \text{ K}$ (Spitzer 1978; Osterbrock & Ferland 2006). If we adopt $T = 8000 \text{ K}$ and 20000 K , we find $\alpha^{(2)} = 3.1 \times 10^{-13}$ and $1.4 \times 10^{-13} \text{ cm}^3 \text{ s}^{-1}$, respectively. The temperature dependence of $\alpha^{(2)}$ does not change our conclusions as long as we assume a typical gas temperature $\sim 10000 \text{ K}$ in H II regions.

for \mathcal{D} and do not follow the time evolution of \mathcal{D} in order to avoid uncertainty in the parameters concerning the chemical evolution models.

From the equations in Sects. 4.1 and 4.2, we can infer the qualitative behavior of r_i as a function of \dot{N}_{ion} . As \dot{N}_{ion} increases, r_S and τ_{Sd} increase (Eqs. 2 and 7) with $\propto \dot{N}_{\text{ion}}^{1/3}$. Inspection of Eq. (4) suggests that if $\tau_{\text{Sd}} \gtrsim 1$, y_i drops in a very sensitive manner with an increase of τ_{Sd} because of the exponential dependence. Thus, if $\tau_{\text{Sd}} \gg 1$, r_i increases only slightly with \dot{N}_{ion} because y_i decreases significantly. On the contrary, $y_i \sim 1$ if $\tau_{\text{Sd}} < 1$, since the dust extinction is not severe. In this case, r_i is roughly proportional to $\dot{N}_{\text{ion}}^{1/3}$.

4.3. Dust-to-gas ratio, metallicity, and filling factor

It is important to realize that \mathcal{D} in τ_{Sd} (Eq. 7) should not be interpreted strictly as a dust-to-gas ratio dependent on metallicity. As implied by Fig. 1, the ionized gas must be clumpy, with concentrations of dense gas embedded in a more tenuous medium (Sect. 2.3). Following Kennicutt (1984) and Osterbrock & Flather (1959), we assume that the emission (and mass) of the ionized gas is dominated by the dense clumps. In this case, the much less dense inter-clump region would provide a negligible contribution to the gas emission and mass. Implicit in this assumption is the optically-thin nature of the clumps (c.f., Giammanco et al. 2004). Therefore, the rms formulation of our models together with the assumption of a uniform distribution would dictate the introduction of a gas volume filling factor δ . Eq. (7) then becomes:

$$\tau_{\text{Sd}} = 0.87 \left(\frac{\mathcal{D}}{6 \cdot 10^{-3}} \right) (\delta^{-1/6}) \left(\frac{n_H}{10^2 \text{ cm}^{-3}} \right)^{1/3} \left(\frac{\dot{N}_{\text{ion}}}{10^{48} \text{ s}^{-1}} \right)^{1/3}, \quad (8)$$

Because only a fraction of the volume δ ($\delta^{1/3}$ of the path length) is occupied by the dense gas, a factor of $\delta^{-1/6}$ must be introduced: $\tau_{\text{Sd}} \propto n_H^{\text{dense}} (\delta^{1/3} r_S) \propto n_H^{\text{rms}} \delta^{-1/2} \delta^{1/3} r_S \propto n_H^{\text{rms}} r_S \delta^{-1/6}$ (“rms” and “dense” distinguish between the rms density and the density in the clumps). The rather mild dependence on δ means that a filling factor of 0.001 would cause only an increase of a factor of 3 in τ_{Sd} .

For convenience, we define the dust-to-gas ratio + filling factor normalized to the solar neighborhood value, κ , as

$$\kappa \equiv \delta^{-1/6} \mathcal{D} / \mathcal{D}_{\odot}. \quad (9)$$

In our models, we have assumed a uniform dust distribution within the H II region, since we have maintained a constant dust-to-gas ratio + filling factor. However, because of stellar winds or grain evaporation, the central cavity surrounding the star cluster could be devoid of dust (e.g., Natta & Panagia 1976; Inoue 2002). In Galactic H II regions excited by single stars, volumes with sizes $\sim 0.5 - 0.8 r_S$ can be dust-free, which would imply dust filling factors as low as $\sim 40\%$. Because of grain destruction effects and strong stellar winds, the dust-free volumes could be even larger in extragalactic H II regions ionized by massive compact star clusters with $10^3 - 10^4$ O stars. In this case, we can still use our formulation, but should interpret the “effective” dust-to-gas ratio κ as being small because of the central cavity. Thus, as mentioned above, the interpretation of small κ is not unique: it could be due either to a low dust content, a relatively high gas filling factor, or to a non-uniform dust distribution caused perhaps by a dust cavity. It is likely that all three mechanisms contribute to the meaning of κ in our formalism.

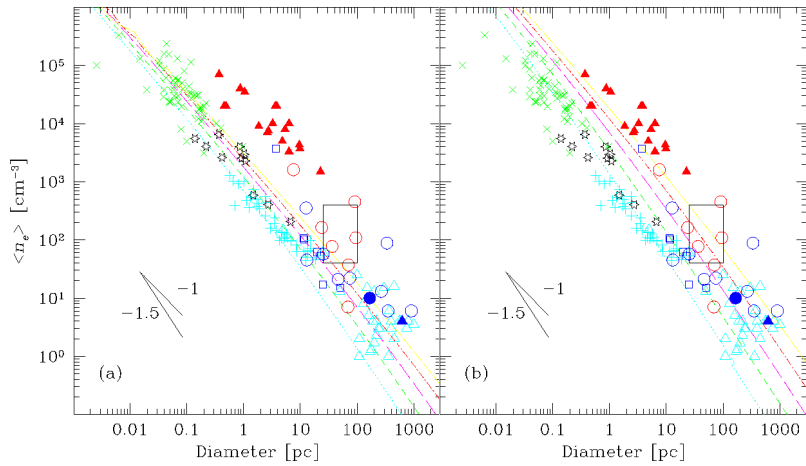


Fig. 3. Relation between the rms electron number density $\langle n_e \rangle$ and the ionization diameter D_i for various samples. Symbols are as in Fig. 2. In addition to the observational data, some theoretical predictions for the static models are shown in each panel: (a) Left panel: the dotted (cyan), short-dashed (green), long-dashed (magenta), dot-dashed (red), and dot-long-dashed (yellow) lines present the results with $\dot{N}_{\text{ion}} = 10^{49}, 10^{50}, 10^{51}, 10^{52},$ and 10^{53} s^{-1} , respectively. A Galactic dust-to-gas ratio + filling factor ($\kappa = 1$) is assumed. (b) Right panel: same as Panel (a) but with $\kappa = 0.1$. The regression slopes corresponding to $n_e \propto D_i^{-1}$ and $n_e \propto D_i^{-1.5}$ are also presented in the lower-left corner in each panel.

4.4. Results

In Fig. 3, the results of the static models are plotted over the observational samples for various \dot{N}_{ion} . Hirashita et al. (2001) suggest that $\dot{N}_{\text{ion}} = 3 \times 10^{49} \text{ s}^{-1}$ on average for Galactic H II regions. Indeed $\dot{N}_{\text{ion}} \sim 10^{49} - 10^{50} \text{ s}^{-1}$ is consistent with the Galactic H II region sample as shown in Fig. 3a. In Fig. 3a, the dust-to-gas ratio is assumed to be Galactic ($\kappa = 1$), while in Fig. 3b, $\kappa = 0.1$ to take into account the relatively low-metallicity of the *HST* sample (Table 2). As shown in Fig. 3a, the size–density relation is relatively insensitive to the change of \dot{N}_{ion} . The reason for this is described in the last paragraph in Sect. 4.2; since $\tau_{\text{sd}} \gg 1$, the increase of r_s with \dot{N}_{ion} is compensated by the decrease of y_i , and as a result, r_i increases only slightly.

Because of this weak dependence of r_i on \dot{N}_{ion} , it is extremely difficult to explain the data of some BCDs, unless we assume an extremely large \dot{N}_{ion} . However, the size–density relation of the extragalactic sample, especially that of the BCDs, is readily explained if we assume a lower dust-to-gas ratio typical of the BCD sample ($\kappa = 0.1$), as shown in Fig. 3b. For this value of dust-to-gas ratio, τ_{sd} is typically $\lesssim 1$, and r_i increases almost in proportion to $\dot{N}_{\text{ion}}^{1/3}$.

Because the size–density relation implies a constant ionized gas column density, as outlined in the Introduction, we might instead expect that the data would be consistent with constant τ_{di} , the dust optical depth within the ionization radius. To test this, because the dust content is expected to decrease with decreasing metallicity, we should correct the inferred ionized gas column densities for the different metal abundances of the samples. Fig. 4 shows the ionized gas column densities multiplied by their oxygen abundance relative to solar plotted against region diameter. This correction assumes that $\kappa \propto Z/Z_\odot$, where Z is metallicity or oxygen abundance. The horizontal lines⁴ correspond to constant τ_{di} of 0.2, 1, 2, 5, and 10. For these calculations of τ_{di} , \dot{N}_{ion} ranged from 10^{48} to 10^{53} s^{-1} , and electron densities $\langle n_e \rangle$ from 10^{-2} to 10^6 cm^{-3} . A large optical depth of $\tau_{\text{di}} \sim 10$ is only possible for large ionization radii achieved with high values of \dot{N}_{ion} ($\sim 10^{52} - 10^{53} \text{ s}^{-1}$) and high densities ($\langle n_e \rangle \sim 10^4 - 10^6 \text{ cm}^{-3}$). This is why the $\tau_{\text{di}} = 10$ horizontal line is shorter than the others. Conversely, the low optical depth $\tau_{\text{di}} = 0.2$ value can only be achieved for low values of \dot{N}_{ion} and low densities, ($\dot{N}_{\text{ion}} \sim 10^{48} - 10^{50} \text{ s}^{-1}$, $\langle n_e \rangle \sim 10^{-2} - 1 \text{ cm}^{-3}$). This is why the $\tau_{\text{di}} = 0.2$ line lies at large diameters.

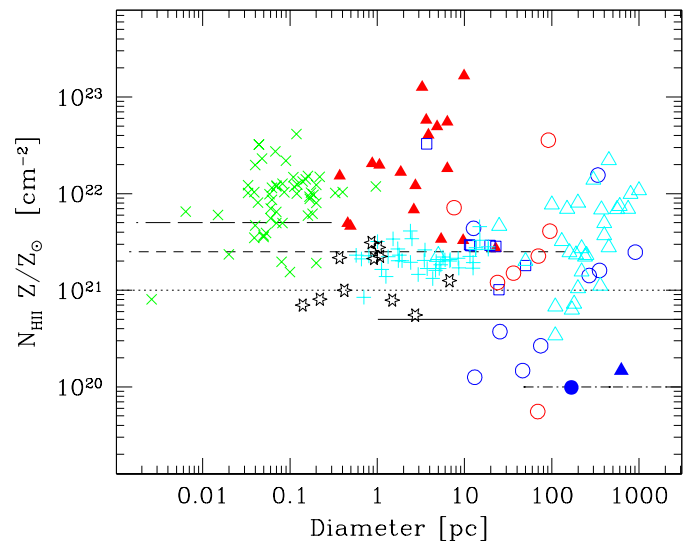


Fig. 4. Ionized gas column densities (cm^{-2}) vs. diameter (pc). The ionized gas column densities have been multiplied by their oxygen abundance relative to solar, assuming the Anders & Grevesse (1989) calibration. Constant τ_{di} are plotted as horizontal lines: $\tau_{\text{di}} = 0.2$ (dot-dashed), 1 (solid), 2 (dotted), 5 (short-dashed), and 10 (long-dashed). Symbols are as in Fig. 2.

It is clear from Fig. 4 that the corrected data are also inconsistent with constant τ_{di} . Moreover, a linear correction of dust column density (or optical depth τ_{di}) for metallicity does not align all the samples. Hence, such a correction is apparently either insufficient or wrong, when considering the dust content of low-metallicity SF regions, at least in the context of these simple models.

The above implies that the size–density relation is not a sequence of either \dot{N}_{ion} or τ_{di} . Rather it is probable that the relation should be considered with variable \dot{N}_{ion} . This means that we should assess how \dot{N}_{ion} evolves if we insist that the entire sample should be explained by a single “unified” sequence. Thus, in the following we include the time variation of \dot{N}_{ion} into our model, and calculate the consequent variations in density and size.

5. Evolutionary models

The treatment used for the evolution of an H II region is based on our previous paper, Hirashita & Hunt (2006, hereafter HH06),

⁴ In our static model, the corrected column densities correspond to $4.9 \times 10^{20} \tau_{\text{di}} \text{ cm}^{-2}$, assuming a Galactic dust-to-gas ratio of 6×10^{-3} (see Appendix A).

where we treat the evolution of the number of ionizing photons emitted per unit time (\dot{N}_{ion}) under a given star formation history. We extend our models to include the effect of grains according to A04. Indeed, as shown below, dust absorption of ionizing photons significantly reduces the size of H II regions especially for compact H II regions (Sect. 7.1). We describe our models in the following.

5.1. Star formation rate

We assume a spherically symmetric uniform SF region with initial hydrogen number density, n_{H0} , and available gas mass for the star formation, M_{gas} . Following HH06, we relate the star formation rate (SFR) with the free-fall time of gas. The free-fall time, t_{ff} , is evaluated as

$$t_{\text{ff}} = \frac{4.35 \times 10^7}{\sqrt{n_{\text{H0}}}} \text{ yr}. \quad (10)$$

Then, the SFR, $\psi(t)$, is estimated with the gas mass divided by the free-fall time as

$$\begin{aligned} \psi(t) &= \frac{\epsilon_{\text{SF}} M_{\text{gas}}}{t_{\text{ff}}} f(t) \\ &\simeq 0.230 \left(\frac{\epsilon_{\text{SF}}}{0.1} \right) \left(\frac{M_{\text{gas}}}{10^7 M_{\odot}} \right) \left(\frac{n_{\text{H0}}}{100 \text{ cm}^{-3}} \right)^{1/2} f(t) M_{\odot} \text{ yr}^{-1}, \quad (11) \end{aligned}$$

where ϵ_{SF} is the star formation efficiency assumed to be 0.1 throughout this paper (HH06), M_{gas} is the total gas mass available in the SF region, and the dimensionless function $f(t)$ specifies the functional form of the SFR. We set the zero point of time t at the onset of star formation in the SF region. We investigate the following functional form for $f(t)$:

$$f(t) = \begin{cases} \exp(-t/t_{\text{g}}) & \text{if } t \geq 0, \\ 0 & \text{if } t < 0, \end{cases} \quad (12)$$

where we define the gas consumption timescale t_{g} as

$$t_{\text{g}} = t_{\text{ff}} / \epsilon_{\text{SF}}. \quad (13)$$

We will refer to this form of the SFR as ‘‘exponentially decaying’’. In order to examine the effects of continuous (not decaying) input of ionizing photons, we also adopt another functional form for the SFR called ‘‘constant SFR’’:

$$f(t) = \begin{cases} 1 & \text{if } t \geq 0, \\ 0 & \text{if } t < 0 \text{ or } t > t_{\text{g}}, \end{cases} \quad (14)$$

We stop the calculation at $t = t_{\text{g}}$ in the constant SFR, since after this time the effect of gas consumption should modify the density structure around the ionizing source.

5.2. Evolution of ionizing photon luminosity

The evolution of the number of ionizing photons emitted per unit time, \dot{N}_{ion} , is calculated by (HH06)

$$\dot{N}_{\text{ion}}(t) = \int_0^{\infty} dm \int_0^{\tau_m} dt' Q(m) \phi(m) \psi(t - t'), \quad (15)$$

where τ_m is the lifetime of a star with mass m , $Q(m)$ is the number of ionizing photons emitted by a star with mass m per unit time, and $\phi(m)$ is the initial mass function (IMF). We assume a Salpeter IMF $\phi(m) \propto m^{-2.35}$ (Salpeter 1955) with stellar mass range of 0.1–100 M_{\odot} . The functional form of the SFR $\psi(t)$ is

specified in Sect. 5.1. We use the fitting formulae of Schaerer (2002) for τ_m and $Q(m)$. We adopt $Z = 0$ (zero metallicity) for the stellar properties following HH06. If we adopt solar metallicity, \dot{N}_{ion} decreases by a factor of ~ 2 for a given stellar mass, but the decrease of \dot{N}_{ion} for metal-rich stars can be compensated if we assume ~ 2 times larger SFR. In fact, after taking into account the different SFR and initial gas mass, our results are comparable to those in Starburst 99 (Leitherer et al. 1999).

5.3. Radius of the ionized region

In order to treat the range of evolution variations from deeply embedded H II regions to normal H II regions, it is crucial to include pressure-driven expansion of H II regions. We adopt a simple analytical approximation based on HH06. Here, we newly include the effect of dust, since A04 have shown that the dust extinction significantly reduces the radius of compact H II region.

We divide the growth of an H II region into two stages: the first stage is the growth of ionizing front due to the increase of ionizing photons, and the second is the pressure-driven expansion of ionized gas. The expansion speed of ionizing front in the first stage is simply estimated by the increasing rate of the ionization radius (Eq. 5). We denote the Strömrgren radius under the initial density as r_{S0} , which is estimated by using Eq. (1) with $n_{\text{H}} = n_{\text{H0}}$. Because of dust extinction, the ionization radius r_{i} is reduced by a factor of y_{i} , which is determined by solving Eq. (4), where τ_{sd} is evaluated by Eq. (7) with a given \mathcal{D} (or κ). The ionization radius r_{i} and τ_{di} are estimated by Eqs. (5) and (6), respectively.

Initially, the increase of r_{i} is caused by the accumulation of ionizing stars. Roughly speaking, as long as \dot{r}_{i} (the increase rate of the ionization radius) is larger than the sound speed of ionized gas, C_{II} (we assume $C_{\text{II}} = 10 \text{ km s}^{-1}$ in this paper), the ionizing front propagates before the system responds hydrodynamically. Therefore, we neglect the hydrodynamical expansion if $\dot{r}_{\text{i}} > C_{\text{II}}$, and adopt the fixed density n_{H0} .

Once $\dot{r}_{\text{i}} < C_{\text{II}}$ is satisfied, pressure-driven expansion is treated. Since the density evolves, we calculate the Strömrgren radius r_{S} under the current density n_{H} by using Eq. (1). In this situation, the growth of the ionizing region is governed by the pressure of ionized gas and the luminosity change of the central stars has only a minor effect. Therefore, the following equation derived by assuming a constant luminosity (A04) approximately holds:

$$\left(\frac{\dot{r}_{\text{i}}}{C_{\text{II}}} \right)^2 = \frac{\rho_{\text{II}}}{\rho_{\text{I}}} \left[1 - \frac{\rho_{\text{II}}}{\rho_{\text{I}}} g(\tau_{\text{di}})^{-2} \right]^{-1}, \quad (16)$$

where ρ_{I} and ρ_{II} are the gas densities outside and inside of the ionized region, respectively, and the function $g(\tau_{\text{di}})$ is defined as

$$g(\tau_{\text{di}}) = \frac{3}{\tau_{\text{di}}^3} (2e^{-\tau_{\text{di}}} - 2 + 2\tau_{\text{di}} - \tau_{\text{di}}^2 + \tau_{\text{di}}^3). \quad (17)$$

The density ratio $\rho_{\text{II}}/\rho_{\text{I}}$ is estimated by (A04)

$$\frac{\rho_{\text{II}}}{\rho_{\text{I}}} \simeq \left(\frac{r_{\text{i0}}}{r_{\text{i}}} \right)^{3/2} \left(\frac{\tau_{\text{di}}}{\tau_0} \right)^{3/2} \left[\frac{-2 + e^{\tau_0} (2 - 2\tau_0 + \tau_0^2)}{-2 + e^{\tau_{\text{di}}} (2 - 2\tau_{\text{di}} + \tau_{\text{di}}^2)} \right], \quad (18)$$

where r_{i0} is evaluated by the Strömrgren radius under the current ionizing photon luminosity and the initial gas density n_{H0} , and τ_0 is the dust optical depth through r_{i0} under density ρ_{I} . Since n_{H} is defined in the ionized region, we relate it with ρ_{II} as

$$\rho_{\text{II}} = \mu m_{\text{H}} n_{\text{H}}, \quad (19)$$

where μm_{H} is the gas mass per hydrogen atom. The density in the neutral region is assumed to be constant:

$$\rho_1 = \mu m_{\text{H}} n_{\text{H}0}. \quad (20)$$

Eqs. (16) and (18) are numerically integrated to obtain r_1 as a function of t .

The above pressure-driven expansion is treated as long as $d(y_i r_S)/dt > 0$. When the SFR declines significantly, r_S begins to decrease. Thus, $d(y_i r_S)/dt < 0$ may be satisfied at a certain time. When $d(y_i r_S)/dt < 0$, $r_i = y_i r_S$ is adopted with fixed n_{H} ; that is, we finish treating the dynamical expansion.

6. Initial conditions and results

6.1. Active and passive star formation

We have argued in previous papers that star formation at low metallicities can proceed in two ways: one “active” mode in which stars form in dense, compact complexes, and the other “passive” mode where star formation occurs over more diffuse and extended regions. The size–density relation presented here for extragalactic H II regions naturally lends itself to the active/passive dichotomy (see also Hunt et al. 2003). Dense regions tend also to be compact, while less dense ones are more extended. Here we examine these “active” and “passive” cases. In HH06, SBS 0335–052 was used as a prototype of the “active” mode, while IZw 18 the “passive” one. This representation was based mainly on the radio continuum results for both galaxies (Hunt et al. 2004; Hunt et al. 2005). Their linear emission measures differ by 3 orders of magnitude, and the resulting densities by a factor of 10. However, even in the optical, the electron densities inferred from the [S II] line ratios differ by a factor of 5 or so (SBS 0335–052 has $n_e \sim 400\text{--}600\text{ cm}^{-3}$, and IZw 18 $n_e \sim 100\text{--}120\text{ cm}^{-3}$, see Table 2). The $\langle n_e \rangle$ of SBS 0335–052 calculated in this paper (Table 2) is much lower than that adopted in HH06 ($n_e \sim 400\text{--}600\text{ cm}^{-3}$; Izotov et al. 1999). As mentioned in Sect. 2 (see also Kennicutt 1984; Rozas et al. 1998), because of clumpiness the densities from the [S II] lines tend to be significantly higher than the $\langle n_e \rangle$. The “active” nature of some BCDs therefore may not emerge in the optical, at least with the rms densities we have adopted here. However, if a BCD can be classified as “active”, when observed in the radio, it would have a compact, dense (or ultra-dense) H II region (see also Sect. 6.2).

Here, for consistency, we examine “active” and “passive” cases by adopting similar initial conditions to those in HH06: the active case is modelled by the so-called “compact model”, and the passive one by the “diffuse model”. Appropriate initial densities are $n_{\text{H}0} \sim 10^3\text{--}10^4\text{ cm}^{-3}$ for the compact model and $n_{\text{H}0} \sim 10^2\text{ cm}^{-3}$ for the diffuse model (HH06). In addition, we also adopt a denser model as a “super-active” class to explain the extragalactic radio sample, and call this model the “dense model”. For all cases, the gas mass is fixed as $M_{\text{gas}} = 10^7 M_{\odot}$, which is similar to the value adopted in HH06. We calculate the evolution of the size–density relation of ionized region for the continuous/burst star-formation histories (Sect. 5.1).

We also examine the dependence on κ , by setting $\kappa = 0, 0.1$, and 1 for dust-free, dust-poor, and dust-rich (Galactic dust-to-gas ratio) cases, respectively. These cases also correspond to varying degrees of dust inhomogeneity or gas filling factor, as described in Sect. 4.3. The sizes and densities of H II regions with a dust content corresponding to $\kappa = 0.01$ are not significantly affected by dust (i.e., the results are similar to the case with $\kappa = 0$), except for the dense model as we discuss later in Sect. 7.1.

On the other hand, the effects of dust extinction can be quite pronounced for $\kappa \gtrsim 0.1$.

6.1.1. Dense model

We adopt $n_{\text{H}0} = 10^5\text{ cm}^{-3}$ ($t_{\text{ff}} = 1.4 \times 10^5\text{ yr}$) and $M_{\text{gas}} = 10^7 M_{\odot}$. With these assumptions, the SFR $\psi(t = 0) = 7.3 M_{\odot}\text{ yr}^{-1}$. First we show the evolution of \dot{N}_{ion} in Fig. 5a for the exponentially decaying and constant SFRs. In both SFR scenarios, \dot{N}_{ion} increases as time passes and stars form.

We present the basic evolutionary behavior of the size and density of H II regions, focusing on the effect of dust, which is newly incorporated in this paper. In Figs. 6a and b, we show the time variation of the ionization radius and of the density, respectively, for various κ in the exponentially decaying star formation history. The cases with $\kappa = 0$ (no dust) are the same as those investigated in HH06. The general behavior of pressure-driven expansion is qualitatively similar in all the dust-to-gas ratios, but quantitatively different. The ionization radius decreases as the dust-to-gas ratio increases, because of the absorption of ionizing photons. The density decreases more rapidly in the dustier case, since the expansion speed normalized to the ionization radius is larger (for a smaller regions, the expansion at a given speed decreases the density more rapidly). The evolution of n_{H} and r_1 is quantitatively similar.

6.1.2. Compact model

We adopt $n_{\text{H}0} = 3 \times 10^3\text{ cm}^{-3}$ ($t_{\text{ff}} = 7.9 \times 10^5\text{ yr}$) and $M_{\text{gas}} = 10^7 M_{\odot}$, as before. With these values for the compact model, the SFR $\psi(t = 0) = 1.3 M_{\odot}\text{ yr}^{-1}$. First we show the evolution of \dot{N}_{ion} in Fig. 5b for the exponentially decaying and constant SFRs: Up to $t \sim 1\text{ Myr}$, \dot{N}_{ion} increases as stars form. For the exponentially decaying SFR, it begins to decrease at $t \sim 5\text{ Myr}$ because of the death of massive stars, while for the constant SFR, it becomes asymptotically constant because the death of massive stars is compensated by their continuous birth.

We present the evolutionary behavior of the size and density of H II regions in Figs. 6c and d for the exponentially decaying star formation history. These models show similar behavior to the dense models. The increase of r_1 and the decrease of n_{H} stop at a later stage of the evolution because of the exponential decay of the SFR.

The temporal behavior in the constant star formation is very similar to that in the exponentially decaying one. The difference is that n_{H} and r_1 continue to decrease and increase, respectively, because the SFR does not decay.

6.1.3. Diffuse model

For the initial density and the radius, we assume $n_{\text{H}0} = 100\text{ cm}^{-3}$ ($t_{\text{ff}} = 4.4 \times 10^6\text{ yr}$) and $M_{\text{gas}} = 10^7 M_{\odot}$, as above. In this case, for the diffuse model, the SFR $\psi(t = 0) = 0.2 M_{\odot}\text{ yr}^{-1}$. The evolution of \dot{N}_{ion} is shown in Fig. 5c for the exponentially decaying and constant SFRs: around 12 Myr , \dot{N}_{ion} is, respectively, $6 \times 10^{52}\text{ s}^{-1}$ and $8 \times 10^{52}\text{ s}^{-1}$. The behavior of \dot{N}_{ion} in the diffuse models as a function of time is qualitatively the same as that in the compact models (Sect. 6.1.2), but with a different SFR. We present the basic evolutionary behavior of the size and density of H II regions for the diffuse models with various dust-to-gas ratios in Figs. 6c and d for the exponentially decaying star formation history. The cases with $\kappa = 0$ (no dust) are the same as those investigated

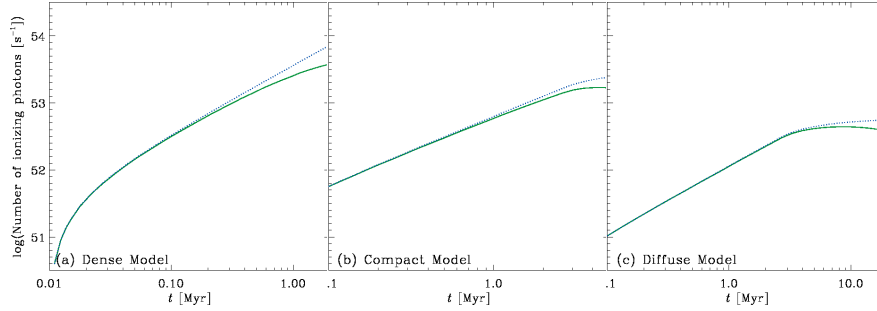


Fig. 5. Time evolution of the number of ionizing photons emitted per unit time (\dot{N}_{ion}). The dense (Panel a), compact (Panel b), and diffuse (Panel c) models are adopted. The solid and dotted lines in each panel correspond to the exponentially decaying and constant star formation rates, respectively.

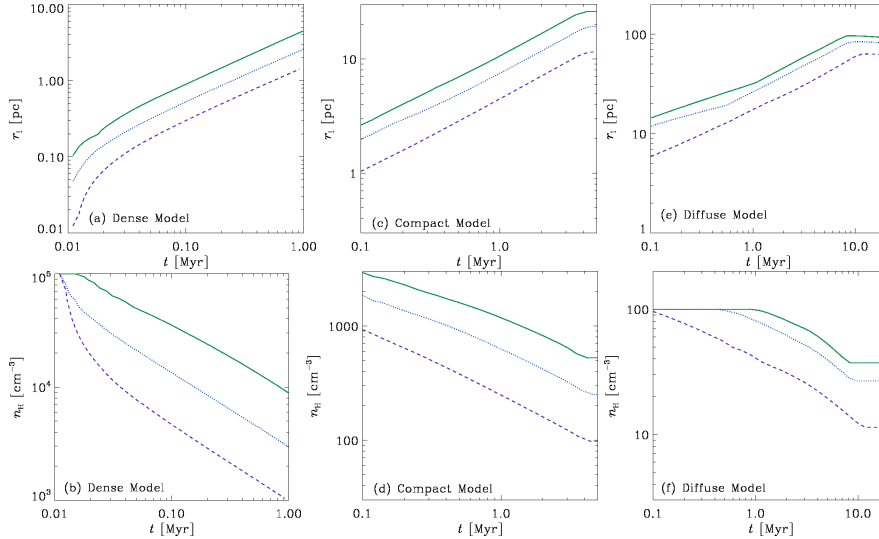


Fig. 6. Time evolution of the ionization radius (r_i ; Panels a, c, and e) and the hydrogen number density (n_{H} ; Panels b, d, and f). The dense (Panels a and b), compact (Panels c and d), and diffuse (Panel c and d) models are adopted with various dust-to-gas ratio normalized to the Galactic value, κ . The solid, dotted, and dashed lines correspond to $\kappa = 0, 0.1, \text{ and } 1$, respectively. The exponentially decaying star formation rate is adopted.

in HH06. For the dependence on the dust-to-gas ratio, the same qualitative discussion as in Sect. 6.1.2 holds.

The increase of r_i and the decrease of n_{H} stop for the same reason as in the compact models. The time evolution in the constant star formation history is very similar to those in the exponentially decaying one, but n_{H} and r_i do not stop decreasing and increasing, respectively.

6.2. Evolutionary tracks on the size–density relation

In Figs. 7a and b, we show the time evolution of the ionized region on the size–density diagram for the exponentially decaying SFR and the constant SFR, respectively. For comparison with the data, we show the diameter of the ionized region, D_i :

$$D_i = 2r_i. \quad (21)$$

Below we discuss the results of the three models.

6.2.1. Specific models

We observe from Fig. 7 that the *dense models* reproduce the data points of the *radio sample*. This means that the radio sample can be understood as an extension of the “active” mode of star formation toward higher density. However, if a Galactic dust-to-gas ratio ($\kappa = 1$) is assumed, the predicted sizes are smaller than those of the radio sample. This implies that the effects of dust extinction are suppressed because of an intrinsically low dust content, a relatively high gas filling factor, or a non-homogeneous dust distribution, but in a way that is not strictly related to metallicity.

Our models are based on the same gas mass, $10^7 M_{\odot}$, in the dense, compact, and diffuse models. This implies that the

star formation activity traced by the radio sample cannot be neglected compared with that traced by the *HST* (optical) sample. As shown later in Sect. 7.1, the fraction of ionizing photons absorbed by dust tends to be larger in denser regions. Thus, although they are potentially important to the total star formation activity, compact and dense H II regions such as we have assembled in the radio sample would tend to be overlooked because of dust extinction.

Fig. 7 shows that the evolutionary tracks of the compact models in the size–density diagram explain the upper part of the *HST* sample with ages of ~ 3 Myr. Thus, the size and density of the “active” class can be explained with the initial conditions of the *compact model*, while as shown below, those of the “passive” class can be reproduced with the less dense initial conditions of the *diffuse model*. This is consistent with the picture that “active” and “passive” star formation processes originate from dense and diffuse SF regions, respectively (Hirashita & Hunt 2004; HH06).

The different classes are also distinguished by different effects of dust extinction. This is shown in Fig. 8, which presents the evolution of the dust optical depth, τ_{di} , for the different classes of models. It can be seen that τ_{di} is not a linear function of κ ; if κ increases, τ_{sd} increases with a fixed values of n_{H} and \dot{N}_{ion} (Eq. 7), but y_i decreases (Eq. 3). As a result, the product $\tau_{\text{di}} = y_i \tau_{\text{sd}}$ is subject to these competing effects. In particular, if $\tau_{\text{di}} \gtrsim 1$, this nonlinearity becomes significant. This is why τ_{di} changes only by a factor of 8 under a change of κ by two orders of magnitude in the dense model. In other words, if dust extinction dominates, the size–density relation is expected to be aligned on a strip with $1 \lesssim \tau_{\text{di}} \lesssim 10$, although we should also consider the possibility that some diffuse regions have low dust optical depth if $\kappa \lesssim 0.01$ is appropriate.

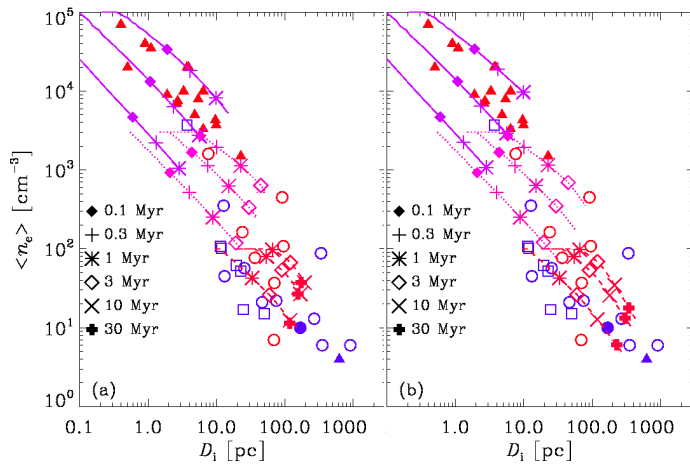


Fig. 7. Relation between the rms electron number density ($\langle n_e \rangle$) and the ionization diameter D_i for **a)** the exponentially decaying SFR and **b)** the constant SFR. The dense, compact, and diffuse models are shown by solid, dotted, and dashed lines, respectively, and the three classes for each model correspond to $\kappa = 0.01$ (top), 0.1, and 1 (bottom). The ages along the model curves are denoted by different symbols as marked. The data of the radio sample and the *HST* sample are shown with the same symbols as in Fig. 2

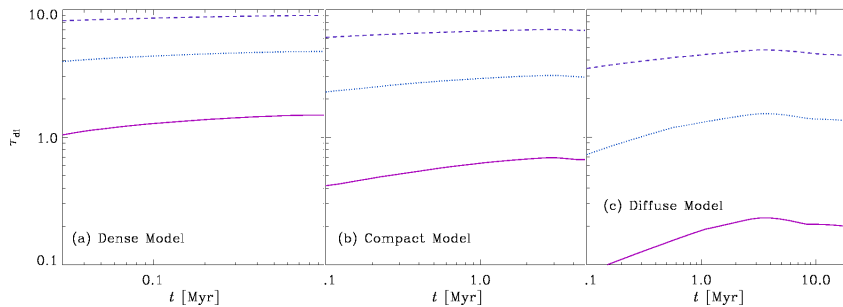


Fig. 8. Evolution of τ_{di} (the dust optical depth over the ionization radius). The solid, dotted, and dashed dotted lines present the results with $\kappa = 0.01$, 0.1, and 1, respectively. The models adopted are **a)** dense model, **b)** compact model, and **c)** diffuse model. The exponentially decaying SFR is adopted in each model.

6.2.2. Summary of the evolutionary tracks

By examining the above three cases, we have inferred that very compact dense H II regions such as the radio sample, compact H II regions in “active” BCDs, and diffuse H II regions in “passive” BCDs are different populations which have emerged because of different initial densities. Our models also suggest that denser regions suffer more from the effects of dust than less dense ones; as shown in Fig. 8, “active” and “passive” star formation modes are characterized by different dust optical depths.

Contrary to the expectation at the end of Sect. 4.4, the radio and *HST* extragalactic samples cannot be reproduced with a single initial condition. Rather we should consider that we are seeing an “envelope” of individual evolutionary tracks of H II regions with diverse initial densities. The concept of “envelope” naturally suggests that we selectively observe the end points of the evolution: i.e., we tend to sample “active” SF regions with young ages of an order of Myr, while we observe “passive” regions with 10 Myr or older ages. In this sense, the observed size–density relation of extragalactic H II regions can be taken as an age sequence, although the relation contains different populations starting from different initial densities. The extreme youth of “super-active” (extremely dense) regions is also supported by the typical rising thermal radio spectrum from free-free gas absorption (Cannon & Skillman 2004; HH06; HH06 also argue that the initial density is important for the rising spectrum).

As mentioned before (Sect. 3.2), some of the galaxies in the *HST* sample are also present in the radio sample, as (ultra-)dense radio H II regions. Hence, it may not only be a question of evolution, but rather also of what the observations are probing. It seems that the more finely some H II regions are probed, the smaller and more dense they appear, even in the same source. The H II region in NGC 5253 has a density of 7500–40000 cm^{-3} if observed with a radio interferometer, but $\sim 300 \text{ cm}^{-3}$ with an optical spectrum. The same is true for He 2–10 (3300–

10000 cm^{-3} in the radio and $\sim 500 \text{ cm}^{-3}$ in the optical; Vacca & Conti 1992), II Zw 40 (35000 cm^{-3} in the radio and $\sim 190 \text{ cm}^{-3}$ in the optical), and, as mentioned above, SBS 0335–052 (1500–7900 cm^{-3} in the radio and $\sim 500\text{--}600 \text{ cm}^{-3}$ in the optical). Thus, we propose that there is a hierarchy of size and density. This picture is consistent with that proposed by Kim & Koo (2001), Efremov & Elmegreen (1998) and Elmegreen (2000), and will be further discussed in Sect. 7.4.

7. Discussion

Here we discuss the implications of our results for evaluating star-formation activity from ionizing photons, and examine how the radio and *HST* samples fit into the larger picture of star formation locally and at high redshift.

7.1. The effects of dust

Even in the dust-poor case with $\kappa \lesssim 0.1$, the absorption of ionizing photons by dust is significant, especially in dense regions with $n_{\text{H}} \gtrsim 10^3 \text{ cm}^{-3}$ (see Fig. 7). The effect of dust extinction in the *HST* sample is expected to be smaller than in the radio sample, but it is never negligible according to our results if $\kappa \gtrsim 0.1$. Thus, dust extinction could constrain the size of H II regions in BCDs, just as it does in Galactic H II regions.

The most straightforward way to confirm if dust extinction significantly alters the size–density relation is to overplot on the data the dust optical depth calculated by the models in Sect. 4. For this purpose, we fix the expression for τ_{di} (Eq. 6) to a constant, and then use the appropriate model n_e and radius (r_i) which would give that τ_{di} as an asymptotic value. This is done in Fig. 9 for $\tau_{di} = 4, 7,$ and 10 for $\kappa = 1$ and $\tau_{di} = 1$ for $\kappa = 0.01, 0.1,$ and 1 . This is a similar diagram to Fig. 4, but with the difference that there we corrected the ionized gas column densities

assuming a linear dependence on metallicity. As for Fig. 4, τ_{di} was calculated for densities which varied from 10^{-2} to 10^6 cm^{-3} , and \dot{N}_{ion} from 10^{48} to 10^{53} s^{-1} ; this is the reason that the lines of constant τ_{di} do not extend over all radii and densities.

With a fixed value of κ , large n_e and/or large r_i are necessary to increase the dust optical depth τ_{di} . Thus, increasing τ_{di} moves the line of constant dust optical depth upward and to the right. However, a small value of κ with a fixed τ_{di} shifts the line of constant τ_{di} in the same direction, because for a small value of κ , n_e and/or r_i need to increase in order to keep τ_{di} constant. Therefore, the line of constant dust optical depth depends strongly on the adopted value of κ .

Several salient points emerge from Fig. 9, and from the comparison of Figs. 9 and 4. First, dust is an important factor in most of the H II regions in our sample, both Galactic and extragalactic ones, since $\tau_{\text{di}} \geq 1$ is indicated. While in Galactic H II regions, this is well established (e.g., Gail & Sedlmayr 1979; Melnick 1979; Churchwell et al. 1990), in low-metallicity BCDs the effects of dust have generally been thought to be negligible.

The second point is that in Fig. 9 the data are fairly well approximated by different values of constant τ_{di} (except for the extremely compact and dense radio sample). Fig. 8 shows that τ_{di} predicted by our evolutionary models varies by no more than a factor of two over the gas consumption lifetime. This relative constancy of τ_{di} predicted by our models may be one of the main underlying factors in the size–density relation observed in H II regions.

Thirdly, the correction for metal abundance applied in Fig. 4 does not align the samples (see Sect. 3). The only difference between Fig. 9 and Fig. 4 is the correction for metallicity assuming that $\kappa \propto$ metallicity. The implication is that this correction is not valid, namely that the dust-to-gas ratio is *not* linear with metallicity (see also Lisenfeld & Ferrara 1998; Hirashita et al. 2002).

Finally, the dense (radio) sample can only be approximated by small values of $\kappa \sim 0.01$. Because the mean metal abundance of the radio sample is $\sim 0.22Z_{\odot}$, this low value of κ cannot reflect a low dust-to-gas ratio resulting from a linear variation with metallicity. Instead, it must point either to regions evacuated of dust through stellar winds, or to an intrinsic lack of dust perhaps because of extreme youth. In addition, a relatively high gas filling factor or an inhomogeneous dust distribution with a central cavity could contribute to the small κ . It is likely that all of these alternatives are shaping the properties of these extreme H II regions.

The generally high values of τ_{di} which are consistent with our H II-region samples suggest the possibility that the size of many H II regions is limited by dust absorption of ionizing photons, rather than the consumption of ionizing photons by neutral hydrogen. If dust extinction governs the size of the H II region (we call this situation “extinction-limited”), we would naturally expect a constant column density of H II regions, which is equivalent to a constant dust optical depth under a fixed mass absorption coefficient of dust grains. Natta & Panagia (1976) also derive a dust optical depth of order unity in the Lyman continuum from Galactic H II regions.

To further quantify the effects of dust extinction in our models, we examine the fraction of ionizing photons absorbed by hydrogen. This fraction is denoted as f and the fraction of ionizing photons absorbed by dust becomes $1 - f$. By using y_i determined in Eq. (4), f is expressed as (Spitzer 1978)

$$f = y_1^3. \quad (22)$$

In Fig. 10, we show the evolution of f for the dense, compact, and diffuse models. It is clear that more than half of the ionizing

photons are absorbed by dust even with $\kappa = 0.01$ in the dense model. With $\kappa \geq 0.1$, the dust absorption is generally severe. Thus, we expect that many of the H II regions in BCDs suffer significant dust absorption of ionizing photons. This means that we would grossly underestimate the total mass of massive stars in compact H II regions in BCDs even from radio observations. The effect is even more pronounced for hydrogen recombination lines. Such an effect is indeed observed in SBS 0335–052 (Reines et al. 2008), and more work is needed to establish this for statistically significant samples.

However, as noted in Sect. 4.2, inhomogeneities in the dust distribution affect $f(\tau_{\text{di}})$, which may be larger (smaller) if we consider, for example, a central dust cavity (Natta & Panagia 1976; Inoue 2002). If such a cavity forms efficiently on a timescale of $\sim 10^5$ yr in compact H II regions, f may increase and the above underestimate of the mass of massive stars could be less severe. For further qualitative discussion, one should treat a motion equation of dusty gas, which is left for future work.

In summary, the above estimates of τ_{di} and f imply that the dust grains play a central role in determining the ionization radius. In particular, the small values of f in compact ionized regions indicate that the effect of dust grains significantly reduce the number of ionizing photons and the ionization radius. This means that there could be a large fraction of massive stars which are not traced with radio observations or with hydrogen recombination lines.

7.2. Galactic H II regions

We have shown that the sequence of extragalactic H II regions cannot be understood as a sequence with a constant \dot{N}_{ion} but that it can be interpreted as an “envelope” of various evolutionary tracks starting from diverse initial densities. This may also be true for Galactic H II regions. Some Galactic H II regions are associated with a single massive star, but some may be associated with a forming stellar cluster, for which we can apply the evolution model described in Sect. 5. This may be the reason why a similar size–density relation ($\langle n_e \rangle \propto D_i^{-1}$) fits the Galactic H II regions (Fig. 2).

In any case, in agreement with previous work, our models with constant τ_{di} suggest that dust plays an important role in Galactic H II regions. As shown in Fig. 9, the more compact H II regions are well fit by $\tau_{\text{di}} \sim 10$, while the less compact ones by $\tau_{\text{di}} \sim 2$. Hence, the Galactic H II region sequence could be a sequence of constant τ_{di} . Nevertheless, because high values of τ_{di} are only possible with high densities and large \dot{N}_{ion} , it could be that the most obscured regions are also the most intrinsically luminous, as suggested above.

7.3. “Active” and “passive” BCDs

In Sect. 6, we have shown that it is not possible to reproduce the entire sample of extragalactic H II regions with a single initial condition. Indeed, the two “active”/“passive” star-formation modes proposed by Hunt et al. (2003) and elaborated upon in subsequent papers (Hirashita & Hunt 2004, HH06), could naturally result from different initial densities. The difference in the gas density (and the compactness) explains the variation in far-infrared luminosity and dust extinction (Takeuchi et al. 2003; Hirashita & Hunt 2004; Takeuchi et al. 2005) and in the molecular fraction (Hirashita & Hunt 2004) between the two classes. We had also hypothesized that the “active” class could be associated with the existence of SSCs. This is supported by the

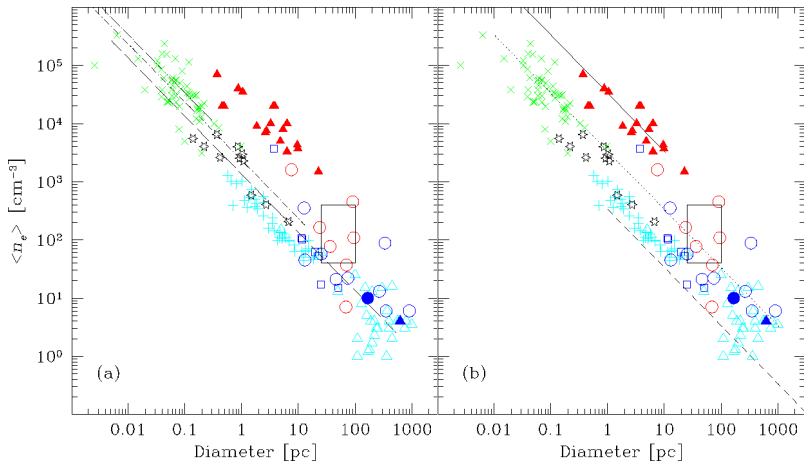


Fig. 9. Size–density relation with a constant dust optical depth τ_{di} . The data symbols are the same as in Fig. 2. (a) Left panel: The long-dashed, dot-short-dashed, and dot-long-dashed lines show $\tau_{\text{di}} = 4, 7,$ and $10,$ respectively, with $\kappa = 1,$ as predicted by the asymptotic behavior of our models. (b) Right panel: The solid, dotted, and dashed lines correspond to $\tau_{\text{di}} = 1$ with $\kappa = 0.01, 0.1,$ and $1,$ respectively.

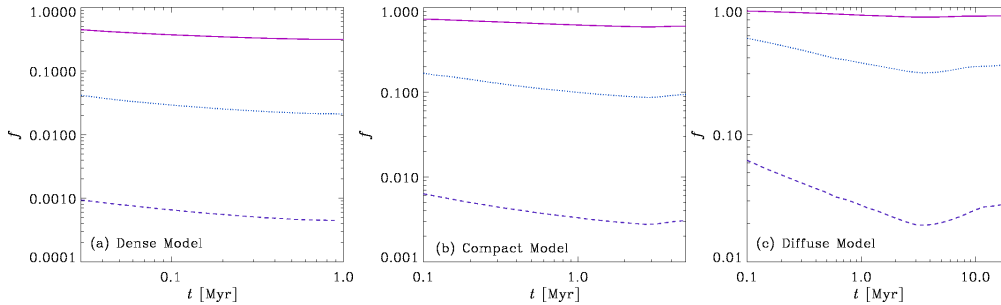


Fig. 10. Evolution of f (the fraction of ionizing photons absorbed by hydrogen). The solid, dotted, and dashed dotted lines present the results with $\kappa = 0.01, 0.1,$ and $1,$ respectively. The models adopted are **a)** dense model, **b)** compact model, and **c)** diffuse model. The exponentially decaying SFR is adopted in each model.

sizes and densities of the known SSCs in the Antennae galaxies (Gilbert & Graham 2007), which are well approximated by the compact models for the active mode of star formation.

In this paper, we have added the radio sample as a dense extreme. The radio sample could be called “super-active” in the sense that their H II regions are denser and more compact than even the “active” BCDs. Indeed, our models imply that they constitute a different population from the *HST* sample, and that they are never detected in the optical because of heavy dust extinction, even at low values of κ . Since a large number of ionizing photons are absorbed by dust grains (Sect. 7.1), even the luminosity of the radio continuum or radio recombination lines underestimates the total mass of massive stars.

The “super-active” mode of star formation seen in the radio sample could also be consistent with the idea that dense conditions foster the formation of SSCs (Billett et al. 2002). In fact, ultra-dense H II regions or radio “supernebulae” have been proposed as SSC progenitors, observed in their very young embedded state (Kobulnicky & Johnson 1999, Johnson et al. 2003, Johnson et al. 2009). This would be consistent with our finding that extreme conditions are necessary to explain the radio sample. The young age predicted by our models would also be consistent with the age of $\lesssim 1$ Myr derived from statistical considerations by Kobulnicky & Johnson (1999).

7.4. Density, time, and size in hierarchical star formation

Elmegreen and collaborators have proposed that there is a timescale–size hierarchy in SF regions (Efremov & Elmegreen 1998, Elmegreen 2000, and references therein). They found a relation between the time difference (Δt) and size and/or separation (S) of clouds and star clusters. We have attempted to assess this trend for the *HST* sample in Fig. 11 by plotting the H β equivalent width ($\text{EW}(\text{H}\beta)$) against the diameter of the ELC as described above. After about 3.1 Myr, $\text{EW}(\text{H}\beta)$ linearly decreases

with starburst age (Leitherer et al. 1999), so we might expect a trend between age and size to be traced by $\text{EW}(\text{H}\beta)$ and ELC diameter. The figure shows a weak negative correlation, formally $\gtrsim 2\sigma$. The two dashed lines, correspond to different methods for determining slopes (Isobe et al. 1990): minimizing the perpendicular distance to the line gives $\text{EW}(\text{H}\beta) \propto D^{-0.23 \pm 0.1}$, and the ordinary-least-squared (OLS) bisector, $\text{EW}(\text{H}\beta) \propto D^{-0.55 \pm 0.1}$. The fitted intercepts at zero size correspond roughly to $\sim 1000 \text{ \AA}$, roughly the $\text{EW}(\text{H}\beta)$ “plateau” for ages younger than ~ 3.1 Myr at oxygen abundances $0.05 Z_{\odot}$. The fitted power-law indices for the *HST* sample are very close to that found by Efremov & Elmegreen (1998) and Elmegreen (2000) of $\Delta t \propto S^{0.33-0.5}$ for molecular clouds and star clusters in the LMC. Hence, even in extragalactic H II regions, there is some (albeit weak) indication that time and size are related, perhaps because of the imprinting of turbulent molecular cloud fragmentation on the star clusters responsible for ionizing the H II gas.

Indeed, the size–density relation of H II regions, $n_e \propto D_1^{-1}$, may be compatible with the above time–size relation. Considering that the timescale of star formation scales with the free-fall timescale (see Sect. 5.1 and Elmegreen 2000), it may be reasonable to assume a scaling relation $\Delta t \propto n_e^{-1/2}$. Combining these two density scaling relations, we obtain $\Delta t \propto D_1^{1/2}$, as long the typical size or separation of SF regions is determined by the size of ionizing radius, $S \sim D_1$. We would thus obtain the same scaling relation as shown by Efremov & Elmegreen (1998) and Elmegreen (2000).

Although our data for H II regions cannot be used to determine star formation activity from small scales to large (galactic) scales (e.g., Elmegreen 2000), we would argue that pressure-driven expansion in H II regions and ionization of the surrounding medium can play a significant role in determining the typical extension or separation of SF complexes. Considering that the dust optical depth affects the ionization radius of H II regions, it

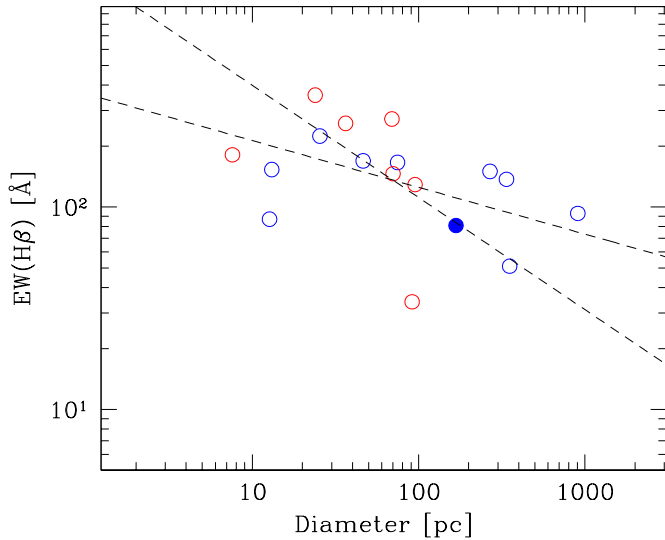


Fig. 11. $H\beta$ equivalent widths (\AA) vs. Diameter (pc) of the SF region in the *HST* sample. Points are shown as in Fig. 1. The regressions correspond to the best-fit lines with slopes of -0.23 (minimizing perpendicular distance from the line), and -0.55 (OLS bisector).

is also possible that dust could be a main factor for determining the typical extension or separation of SF regions.

7.5. Implications for high-redshift star formation

The number density of gas in high-redshift primeval galaxies is theoretically considered to be $\gtrsim 10^3 \text{ cm}^{-3}$ (Norman & Spaans 1997). Therefore, the SF regions in such galaxies may be expected to mimic our compact models. This means that a significant fraction of ionizing photons can be absorbed by dust grains. According to Fig. 10, roughly 1/3 of the ionizing photons are absorbed in the compact model even when $\kappa = 0.01$. A pair-instability supernova originating from a Population III star is expected to supply $\sim 10M_{\odot}$ of dust grains (Nozawa et al. 2003; Schneider et al. 2004); if the baryonic mass of the first object is $\sim 10^5M_{\odot}$ (Tegmark et al. 1997), the dust-to-gas ratio becomes $\sim 10^{-4}$ ($\kappa \sim 10^{-2}$). Thus, $\kappa \sim 10^{-2}$ is reached relatively quickly, and dust extinction becomes important soon after the death of the first Population III stars. Our results also suggest that the radiative transfer of ionizing photons at high z is strongly affected by dust extinction. Thus, the cosmic reionization history should be reconsidered by taking into account the effects of dust extinction.

It is also interesting to consider the starburst populations at lower (but still high) redshifts ($z \lesssim 5$). Although resolving individual dense H II regions is impossible in high- z galaxies, an intense starburst at high z would be expected to produce several giant H II regions or massive ELCs. For example, let us assume a star-forming region whose gas mass is three orders of magnitude larger than that assumed for the BCDs (i.e., $M_{\text{gas}} = 10^{10}M_{\odot}$; note that this is not the total gas mass in the entire galaxy but the gas mass involved in the current star formation episode). With $n_{\text{H0}} \sim 100 \text{ cm}^{-3}$ (typical density for the diffuse model) we can roughly reproduce a typical SFR $\sim 200M_{\odot} \text{ yr}^{-1}$ (Eq. 11) for luminous infrared galaxies (Sanders & Mirabel 1996). If the exponentially decaying SFR is adopted, this model after $t \sim 30 \text{ Myr}$ can also be used to mimic a typical SFR of more mildly

star-forming populations such as Lyman break galaxies and Ly α emitters (e.g., Takeuchi & Ishii 2004; Pirzkal et al. 2007). Moreover, with $n_{\text{H0}} \sim 10^4 \text{ cm}^{-3}$, the SFR roughly becomes a typical value for such extreme starbursts ($\sim 1000M_{\odot} \text{ yr}^{-1}$) as are seen in submillimeter galaxies (e.g., Hughes et al. 1998).

Because the Strömgen radius depends only weakly on \dot{N}_{ion} (Eq. 2), the size of H II regions is only one order of magnitude larger even when the SFR (\dot{N}_{ion} is proportional to SFR) increases by three orders of magnitude. Severe dust extinction would lessen the increase of H II region size. Nevertheless, this implies that high- z starburst population could produce an immense dense H II region whose size ($\gtrsim 100 \text{ pc}$) is an order of magnitude larger than the local (dense) extragalactic H II regions.

In these massive H II regions, if the H II region size becomes larger than 100 pc , pressure-driven expansion ceases to be important. The reason is as follows: pressure-driven expansion occurs on a sound-crossing timescale. Since the sound speed in H II regions is $\sim 10 \text{ km s}^{-1}$, the sound-crossing time over a 100 pc region is 10 Myr , comparable to the typical lifetime of massive stars. Thus, such a giant H II region cannot be sustained long enough for the pressure-driven expansion to modify the ionized-gas density. Consequently, the density of such a giant H II region reflects the initial density averaged over the current H II region size.

7.6. Maximum-intensity starbursts

The “dense” (“super-active”) and “active” star formation modes we have modelled far exceed the empirical *global* star-formation intensity limit of $\sim 45 M_{\odot} \text{ yr}^{-1} \text{ kpc}^{-2}$ found by Meurer et al. (1997). However, recent observations of submillimeter galaxies and quasar hosts at high redshift have discovered “hyper-starbursts” occurring in small regions of $\lesssim 1\text{--}3 \text{ kpc}$ in diameter (e.g., Tacconi et al. 2006, Walter et al. 2009). These kiloparsec-scale starbursts have SFRs per unit area on the order of $100\text{--}1000 M_{\odot} \text{ yr}^{-1} \text{ kpc}^{-2}$, comparable to those of our models. Similar high starburst surface densities are found in Arp 220 but on spatial scales of a few 100 pc (Scoville et al. 1997). With $10^{10} M_{\odot}$ of gas, roughly that in Arp 220, these are roughly the spatial extents predicted by our evolutionary models for massive starbursts, as described in the previous section.

If dust is a principle factor in shaping the observable properties of H II regions and ELCs, then we might expect shorter wavelengths, in particular the ultraviolet, to be unsuitable for sampling SFRs in such objects. This would mean that starburst intensity limits both locally and at high redshift would need to be reassessed at submillimeter or infrared wavelengths where dust reprocessing gives a more accurate picture (see also Gao 2008).

8. Conclusions

We have investigated the size–density relation of extragalactic H II regions, focusing on those in BCDs. Motivated by the similarity of size–density relations of extragalactic H II regions with Galactic ones, we have modelled and examined the size–density relation of ionized regions by considering the effects of dust, star formation history, and pressure-driven expansion of H II regions. The results have been compared with several samples spanning roughly six orders of magnitude in size and density. We have shown that the entire sample set cannot be understood as an evolutionary sequence with a single initial condition. Rather, the size–density relation reflects a sequence with different initial gas densities. Thus, a hierarchical structure of SF regions with various densities is implied.

We have also found that the size of extragalactic H II regions is “dust-extinction limited”, in the sense that the dust absorption of ionizing photons is significant. This naturally explains the observed size–density relation of H II regions as following a constant column density of ionized gas, if the dust-to-gas ratio in H II regions is constant. The dust extinction of ionizing photons is particularly severe over the entire lifetime of the compact radio sample with typical densities of $\gtrsim 10^3 \text{ cm}^{-3}$. This means that the compact radio sample constitutes a different population from the optical samples and that star formation activity in such dense regions would be underestimated or missed entirely if we use the emission from H II regions (hydrogen recombination lines, free-free continuum) as the sole indicators of star formation rate.

Acknowledgements. We would like to humbly dedicate this paper to the memory of Prof. Edwin Salpeter, who provided precious insight during its development. We are also grateful to B. G. Elmegreen, R. C. Kennicutt, and A. K. Inoue for stimulating discussions on the properties of H II regions. Finally, we thank the anonymous referee for useful comments which substantially improved the paper. This research has made use of the NASA/IPAC Extragalactic Database (NED), which is operated by the Jet Propulsion Laboratory, California Institute of Technology, under contract with the National Aeronautics and Space Administration (NASA).

Appendix A: Simple derivation of Eq. (7)

Eq. (7) is derived in Hirashita et al. (2001) based on Spitzer (1978). Here, we present a simpler derivation of Eq. (7).

We start from the optical depth at the threshold wavelength of the Lyman continuum (912 Å) denoted as τ_L :

$$\tau_L \simeq A_{1000}/1.086 = 12.0E_{B-V}, \quad (\text{A.1})$$

where τ_L is approximated with the extinction at $\lambda = 1000$ Å, which is related with the $B - V$ color excess, E_{B-V} , by assuming the Galactic extinction curve (Spitzer 1978). The factor 1.086 is required for the conversion from A_{1000} (the extinction at 1000 Å in units of magnitude) to τ_L . Assuming that the dust-to-gas ratio is the same between the ionized and neutral media (Sect. 4.2), we simply use the proportionality between the color excess and the hydrogen column density derived for the Galactic environment (Spitzer 1978); i.e., we adopt

$$N_H = 5.9 \times 10^{21} E_{B-V} \text{ mag}^{-1} \text{ cm}^{-2}, \quad (\text{A.2})$$

for solar metallicity. Then we obtain

$$\tau_L = 2.03 \times 10^{-21} N_H. \quad (\text{A.3})$$

Next, we estimate τ_{sd} (the dust optical depth for the ionizing photons over a path length equal to the Strömgen radius) introduced in Eq. (4). Noting that the hydrogen column density over the Strömgen radius is given by $N_H = n_H r_S$, we obtain $\tau_L = \tau_{\text{sd}}$ as shown in Eq. (7) after using the expression in Eq. (2). If we consider the optical depth over the ionization radius, $\tau_L = \tau_{\text{di}}$ should be applied.

References

- Anderson, L. D., & Bania, T. M. 2009, *ApJ*, 690, 706
 Anders, E., & Grevesse, N. 1989, *Geochim. Cosmochim. Acta*, 53, 197
 Arthur, S. J., Kurtz, S. E., Franco, J., & Albarrán, M. Y. 2004, *ApJ*, 608, 282 (A04)
 Beck, S. C., Turner, J. L., Kovo, O. 2000, *AJ*, 120, 244
 Beck, S. C., Turner, J. L., Langland-Shula, L. E., et al. 2002, *AJ*, 124, 2516
 Billett, O. H., Hunter, D. A., & Elmegreen, B. G. 2002, *AJ*, 123, 1454
 Buckalew, B. A., Kobulnicky, H. A., & Dufour, R. J. 2005, *ApJS*, 157, 30
 Cannon, J. M., & Skillman, E. D. 2004, *ApJ*, 610, 772
 Churchwell, E., Wolfire, M. G., & Wood, D. O. S. 1990, *ApJ*, 354, 247
 Churchwell, E., & Goss, W. M. 1999, *ApJ*, 514, 188
 Corbin, M. R., Vacca, W. D., Hibbard, J. E., et al. 2005, *ApJ*, 629, L89
 Deeg, H.-J., Brinks, E., Duric, N., Klein, U., & Skillman, E. 1993, *ApJ*, 410, 626
 Dopita, M. A., Fischera, J., Crowley, O., et al. 2006, *ApJ*, 639, 788
 Efremov, Y. N., & Elmegreen, B. G. 1998, *MNRAS*, 299, 588
 Elmegreen, B. G. 2000, *ApJ*, 530, 277
 Foster, T., & MacWilliams, J. 2006, *ApJ*, 644, 214
 Freedman, W. L., Wilson, C. D., & Madore, B. F. 1991, *ApJ*, 372, 455
 Gail, H. P., & Sedlmayr, E. 1979, *A&A*, 77, 165
 Gao, Y. 2008, *Nature*, 452, 417
 Garay, G., & Lizano, S. 1999, *PASP*, 111, 1049
 Garnett, D. R. 2002, *ApJ*, 581, 1019
 Giammanco, C., Beckman, J. E., Zurita, A., & Relaño, M. 2004, *A&A*, 424, 877
 Gies, D. R., & Lambert, D. L. 1992, *ApJ*, 387, 673
 Gilbert, A. M., & Graham, J. R. 2007, *ApJ*, 668, 168
 Gordon, M. A. 1988, *Galactic and Extragalactic Radio Astronomy*, 37
 Guseva, N. G., Izotov, Y. I., Papaderos, P., Fricke, K. J. 2007, *A&A*, 464, 885
 Guseva, N. G., Izotov, Y. I., & Thuan, T. X. 2000, *ApJ*, 531, 776
 Guseva, N. G., Papaderos, P., Izotov, Y. I., et al. 2003, *A&A*, 407, 105
 Guseva, N. G., Papaderos, P., Izotov, Y. I., et al. 2004, *A&A*, 421, 519
 Hachisuka, K., et al. 2006, *ApJ*, 645, 337
 Hirashita, H., & Hunt, L. K. 2004, *A&A*, 421, 555
 Hirashita, H., & Hunt, L. K. 2006, *A&A*, 460, 67 (HH06)
 Hirashita, H., Inoue, A. K., Kamaya, H., & Shibai, H. 2001, *A&A*, 366, 83
 Hirashita, H., Tajiri, Y. Y., & Kamaya, H. 2002, *A&A*, 388, 439
 Hughes, D. H., Serjeant, S., Dunlop, J., et al. 1998, *Nature*, 394, 241
 Hunt, L. K., Dyer, K. K., Thuan, T. X. 2005, *A&A*, 436, 837
 Hunt, L. K., Dyer, K. K., Thuan, T. X., & Ulvestad, J. S. 2004, *ApJ*, 606, 853
 Hunt, L. K., Hirashita, H., Thuan, T. X., Izotov, Y. I., & Vanzi, L. 2003, in *Proceedings of "Galaxy Evolution: Theory and Observations"*, Eds. V. Avila-Reese, C. Firmani, C. Frenk, & C. Allen, *RevMexAA SC (astro-ph/0310865)*
 Hunt, L. K., Vanzi, L., & Thuan, T. X. 2001, *A&A*, 377, 66
 Hunter, D. A., & Hoffman, L. 1999, *AJ*, 117, 2789
 Inoue, A. K. 2002, *ApJ*, 570, 688
 Inoue, A. K., Hirashita, H., & Kamaya, H. 2001, *ApJ*, 555, 613
 Isobe, T., Feigelson, E. D., Akritas, M. G., & Babu, G. J. 1990, *ApJ*, 364, 104
 Izotov, Y. I., Chaffee, F. H., Foltz, C. B., et al. 1999, *ApJ*, 527, 757
 Izotov, Y. I., Chaffee, F. H., Foltz, C. B., et al. 2001a, *ApJ*, 566, 222
 Izotov, Y. I., Chaffee, F. H., & Green, R. F. 2001b, *ApJ*, 562, 727
 Izotov, Y. I., Papaderos, P., Guseva, N. G., et al. 2004, *A&A*, 421, 539
 Izotov, Y. I., Schaerer, D., Blecha, A., Royer, F., Guseva, N. G., & North, P. 2006a, *A&A*, 459, 71
 Izotov, Y. I., Stasińska, G., Meynet, G., et al. 2006b, *A&A*, 448, 955
 Izotov, Y. I., & Thuan, T. X. 1998, *ApJ*, 500, 188
 Izotov, Y. I., & Thuan, T. X. 2004a, *ApJ*, 602, 200
 Izotov, Y. I., Thuan, T. X., & Lipovetsky, V. A. 1994, *ApJ*, 435, 647
 Izotov, Y. I., Thuan, T. X., & Lipovetsky, V. A. 1997, *ApJS*, 108, 1
 Izotov, Y. I., Thuan, T. X., & Stasińska, G. 2007, *ApJ*, 662, 15
 Johnson, K. E., Kobulnicky, H. A., Massey, P., & Conti, P. S. 2001, *ApJ*, 559, 864
 Johnson, K. E., Leitherer, C., Vacca, W. D., & Conti, P. S. 2000, *AJ*, 120, 1273
 Johnson, K. E., Indebetouw, R., & Pisano, D. J. 2003, *AJ*, 126, 101
 Johnson, K. E., Hunt, L. K., & Reines, A. E. 2009, *AJ*, 137, 3788
 Kehrig, C., Vílchez, J. M., Telles, E., et al. 2006, *A&A*, 457, 477
 Kennicutt, R. C., Jr. 1984, *ApJ*, 287, 116
 Kim, K.-T., & Koo, B.-C. 2001, *ApJ*, 549, 979
 Kilian, J. 1992, *A&A*, 262, 171
 Kitayama, T., Yoshida, N., Susa, H., et al. 2004, *ApJ*, 613, 631
 Kniazev, A. Y., Pustilnik, S. A., Masegosa, J., et al. 2000, *A&A*, 357, 101
 Kniazev, A. Y., Pustilnik, S. A., Ugryumov, A. V., & Pramsky, A. G. 2001, *A&A*, 371, 404
 Kobulnicky, H. A., & Johnson, K. E. 1999, *ApJ*, 527, 154
 Kobulnicky, H. A., Kennicutt, R. C., Jr., & Pizagno, J. L. 1999, *ApJ*, 514, 544
 Kobulnicky, H. A., & Skillman, E. D. 1996, *ApJ*, 471, 211
 Kunth, D., & Joubert, M. 1985, *A&A*, 142, 411
 Larson, R. B. 1981, *MNRAS*, 194, 809
 Leitherer, C., et al. 1999, *ApJS*, 123, 3
 Lequeux, J., & Viallefond, F. 1980, *A&A*, 91, 269
 Lisenfeld, U., & Ferrara, A. 1998, *ApJ*, 496, 145
 Martín-Hernández, N. L., van der Hulst, J. M., & Tielens, A. G. G. M. 2003, *A&A*, 407, 957
 Martín-Hernández, N. L., Vermeij, R., & van der Hulst, J. M. 2005, *A&A*, 433, 205
 Massey, P., & Hunter, D. A. 1998, *ApJ*, 493, 180
 Mathis, J. S. 2000, in *Allen's Astrophysical Quantities*, Fourth Edition, ed. A. N. Cox, (Springer, New York), p. 523
 Melnick, J. 1979, *ApJ*, 228, 112
 Mohan, N. R., Anantharamaiah, K. R., & Goss, W. M. 2001, *ApJ*, 557, 659
 Moustakas, J., & Kennicutt, R. C., Jr. 2006, *ApJS*, 164, 81
 Meurer, G. R., Heckman, T. M., Lehnert, M. D., Leitherer, C., & Lowenthal, J. 1997, *AJ*, 114, 54
 Mezger, P. G., & Henderson, A. P. 1967, *ApJ*, 147, 471
 Natta, A., & Panagia, N. 1976, *A&A*, 50, 191
 Norman, C. A., & Spaans, M. 1997, *ApJ*, 480, 145
 Nozawa, T., Kozasa, T., Umeda, H., et al. 2003, *ApJ*, 598, 785
 Noeske, K. G., Guseva, N. G., Fricke, K. J., et al. 2000, *A&A*, 361, 33
 Omukai, K., & Nishi, R. 1999, *ApJ*, 518, 64
 Osterbrock, D. E., & Ferland, G. J. 2006, *Astrophysics of Gaseous Nebulae and Active Galactic Nuclei*, Second Edition (Sausalito: University Science Books)
 Osterbrock, D., & Flather, E. 1959, *ApJ*, 129, 26
 Papaderos, P., Guseva, N. G., Izotov, Y. I., et al. 2006, *A&A*, 457, 45
 Peimbert, M. 1987, in *Star Forming Regions*, ed. M. Peimbert & J. Jugaku (Reidel, Dordrecht), p. 111
 Petrosian, V., Silk, J., & Field, G. B. 1972, *ApJ*, 177, L69
 Pirzkal, N., Malhotra, S., Rhoads, J. E., & Xu, C. 2007, *ApJ*, 667, 49
 Reines, A. E., Johnson, K. E., & Hunt, L. K. 2008, *AJ*, 136, 1415
 Rozas, M., Castaneda, H. O., & Beckman, J. E. 1998, *A&A*, 330, 873
 Russeil, D., Adami, C., & Georgelin, Y. M. 2007, *A&A*, 470, 161
 Salpeter, E. E. 1955, *ApJ*, 121, 161
 Sanders, D. B., & Mirabel, I. F. 1996, *ARA&A*, 34, 749
 Schaerer, D. 2002, *A&A*, 382, 28
 Schneider, R., Ferrara, A., & Salvaterra, R. 2004, *MNRAS*, 351, 1379
 Scoville, N. Z., Yun, M. S., & Bryant, P. M. 1997, *ApJ*, 484, 702
 Shi, F., Kong, X., Li, C., & Cheng, F. Z. 2005, *A&A*, 437, 849

Table 1. Radio sample

Name	d (Mpc)	n_e (cm^{-3})	D (pc)	$12 + \log(\text{O}/\text{H})$	ref. ^{a,b}
He 2–10	10.4	10000	6.4	8.06	1, 9
		3300	6.4		1
I Zw 18	14.6	4	626	7.17	3, 10
II Zw 40	11.1	35000	1.1	8.13	3, 10
M 33	0.84 ^c	3700	3.7	8.78	5, 17
Mrk 8	52.5	20000	3.7	8.51	4, 13
Mrk 33	25.5	9000	1.9	8.40	4, 14
Mrk 1089	54.6	20000	3.9	8.04	4, 12
Mrk 1236	29.6	20000	0.5	8.07	4, 16
NGC 4214n	3.8	70000	0.4	8.22	4, 11
NGC 5253	2.5	7500	2.7	8.17	1, 8
		40000	0.9		2
NGC 6946	5.6	3700	9.9	9.12	5, 15
NGC 253	3.4	10000	3.3	8.88	5, 17
Pox 4	52.5	7000	2.6	7.95	4, 14
SBS 0335–052	53.7	1500	22.7	7.30	6, 10
SBS 0335–052–1	53.7	4300	9.6	7.30	7, 10
SBS 0335–052–2	53.7	7900	5.4	7.30	7, 10
Tol 35	25.2	20000	0.5	8.11	4, 15
VII Zw 19	67.4	5000	4.8	8.71	4, 14

^a References for the radio interferometric observations: 1) Mohan et al. (2001); 2) Turner et al. (2000); 3) Beck et al. (2002); 4) Beck et al. (2000); 5) Johnson et al. (2001); 6) Hunt et al. (2004); 7) Johnson et al. (2009).

^b References for the oxygen abundance: 8) Walsh & Roy (1989); 9) Vacca & Conti (1992); 10) Thuan & Izotov (2005); 11) Kobulnicky & Skillman (1996); 12) Guseva et al. (2000); 13) Shi et al. (2005); 14) Kunth & Joubert (1985); 15) Kobulnicky et al. (1999); 16) Buckalew et al. (2005); 17) Garnett (2002).

^c The distance of M33 is taken from Freedman et al. (1991).

Silich, S., Tenorio-Tagle, G., & Muñoz-Tuñón, C. 2007, *ApJ*, 669, 952
 Spitzer, L., Jr. 1978, *Physical Processes in the Interstellar Medium* (Wiley, New York)
 Tacconi, L. J., et al. 2006, *ApJ*, 640, 228
 Takeuchi, T. T., Hirashita, H., Ishii, T. T., Hunt, L. K., & Ferrara, A. 2003, *MNRAS*, 343, 839
 Takeuchi, T. T., & Ishii, T. T. 2004, *A&A*, 426, 425
 Takeuchi, T. T., Ishii, T. T., Nozawa, T., et al. 2005, *MNRAS*, 362, 592
 Tegmark, M., Silk, J., Rees, M. J., et al. 1997, *ApJ*, 474, 1
 Tenorio-Tagle, G., Muñoz-Tuñón, C., Pérez, E., Silich, S., & Telles, E. 2006, *ApJ*, 643, 186
 Thuan, T. X., & Izotov, Y. I. 2005, *ApJS*, 161, 240
 Thuan, T. X., Izotov, Y. I., & Lipovetsky, V. A. 1997, *ApJ*, 463, 120
 Thuan, T. X., Izotov, Y. I., & Lipovetsky, V. A. 1997, *ApJ*, 477, 661
 Thuan, T. X., Sauvage, M., & Madden, S. 1999, *ApJ*, 516, 783
 Turner, J. L., Beck, S. C., & Ho, P. T. P., 2000, *ApJ*, 532, L109
 Vacca, W. D., & Conti, P. S. 1992, *ApJ*, 401, 543
 Vanzì, L., Hunt, L. K., & Thuan, T. X. 2002, *A&A*, 390, 481
 Walsh, J. R., & Roy, J.-R. 1989, *MNRAS*, 239, 297
 Walter, F., Riechers, D., Cox, P., Neri, R., Carilli, C., Bertoldi, F., Weiss, A., & Maiolino, R. 2009, *Nature*, 457, 699
 Yoshida, N., Abel, T., Hernquist, L., & Sugiyama, N. 2003, *ApJ*, 592, 645
 Zaritsky, D., Kennicutt, R. C., Jr., & Huchra, J. P. 1994, *ApJ*, 420, 87

Table 2. *HST* sample

Name	Dist. ^a (Mpc)	12+ log(O/H) ^b	T_e ^c ($\times 10^4$ K)	n_e ([S II]) ^d (cm^{-3})	$\langle n_e \rangle$ ^e (cm^{-3})	$F_{H\beta}$ ^f ($\times 10^{-14}$ $\text{erg cm}^{-2} \text{s}^{-1}$)	EW(H β) ^g (\AA)	Filter	D^h (pixel)	D^i (pc)	Ref. ^j
(1)	(2)	(3)	(4)	(5)	(6)	(7)	(8)	(9)	(10)	(11)	(12)
Haro 3	18.5	8.34	1.019	180	37	26.4	146	F606W	11.6	70.2	1, 2
He 2-10-A	10.4	8.34	1.120	383	450	261.0	34	F814W	12.1	91.4	3, 4, 5
HS 0822+3542	12.6	7.46	2.000	390	7	0.5	272	F814W	30.2	69.1	2, 6, 7, 8
II Zw 40	11.1	8.13	1.302	190	77	8.5	259	F814W	18.0	36.4	2, 9
I Zw 18-NW	14.6	7.17	1.997	120	10	3.2	81	F814W	35.1	167.8	2, 10
Mrk 59-1	13.4	8.01	1.354	79	13	15.1	150	F606W	27.6	268.7	2, 11
Mrk 71-A	4.4	7.89	1.568	150	163	87.3	357	F814W	7.5	23.9	10, 12
Mrk 209	5.2	7.81	1.561	100	57	14.6	224	F814W	13.4	25.5	2, 10
Mrk 930	74.6	8.06	1.230	58	6	6.9	93	F606W	16.7	905.9	13
Mrk 996	21.7	8.00	1.500	450	108	20.2	129	F791W	6.0	95.2	14
NGC 1140	19.8	8.28	1.024	70	6	6.7	51	F814W	24.5	352.9	1, 9, 15
NGC 1156	6.5	8.39	1.630	30	353	240.0	87	F814W	10.7	12.7	12, 16
NGC 1741-A	54.6	8.12	1.130	120	88	88.9	137	F814W	8.5	337.5	3, 9, 15
NGC 5253-1	2.5	8.17	1.190	290	1603	223.9	181	F814W	8.3	7.6	4, 17
Pox 186	17.5	7.74	1.694	350	36	3.5	375	F814W	4.2	53.8	18
SBS 0335–052	53.7	7.30	2.000	412	10	1.9	230	F791W	3.5	134.4	2, 15, 19, 20
SBS 1415+437	12.8	7.61	1.700	60	22	4.5	166	F791W	8.0	74.7	22
Tol 1214–277	115.6	7.55	1.979	325	7	1.9	290	F814W	4.3	358.2	15, 23
Tol 1924–416a	42.4	7.94	1.390	78	64	9.7	59	F814W	2.0	61.3	24, 25, 26
Tol 65	32.0	7.54	1.732	120	17	2.6	221	F814W	4.3	98.5	23, 27
UGC 4483	5.1	7.58	1.700	100	21	2.2	169	F814W	12.4	46.4	15, 21
UM 311	22.6	8.31	0.970	44	26	10.5	279	F814W	2.7	43.9	13, 15
VII Zw 403	1.5	7.73	1.540	41	45	4.7	153	F814W	12.2	13.1	10, 12, 15

^a Distance from NED.^b Oxygen abundance in ionized gas.^c Electron temperature.^d Electron number density n_e ([S II]) measured from the ratio of $\lambda\lambda 6717, 6731 \text{ \AA}$.^e RMS electron number density $\langle n_e \rangle$ inferred from the H β emission measure with diameters as in Col. 11, corrected for extinction and ionized helium as described in the text.^f H β flux in the spectroscopic slit.^g Equivalent width of H β emission.^h Diameters of brightest star-forming complex as described in the text, without the enlargement factor.ⁱ Diameters of brightest star-forming complex ($1.5\times$ that measured in the continuum) as described in the text.^j Spectroscopic references: 1) Izotov & Thuan (2004b); 2) Thuan & Izotov (2005); 3) Vacca & Conti (1992); 4) Kobulnicky et al. (1999); 5) Johnson et al. (2000); 6) Kniazev et al. (2000); 7) Corbin et al. (2005); 8) Izotov et al. (2006); 9) Guseva et al. (2000); 10) Izotov et al. (1997); 11) Noeske et al. (2000); 12) Hunter & Hoffman (1999); 13) Izotov & Thuan (1998); 14) Thuan et al. (1996); 15) Izotov et al. (2007); 16) Moustakas & Kennicutt (2006); 17) Walsh & Roy (1989); 18) Guseva et al. (2004); 19) Izotov et al. (1999); 20) Izotov et al. (2006); 21) Izotov et al. (1994); 22) Guseva et al. (2003); 23) Izotov et al. (2001b); 24) Guseva et al. (2007); 25) Papaderos et al. (2006); 26) Kehrig et al. (2006); 27) Izotov et al. (2004a); 28) Kniazev et al. (2001).